JGR Space Physics

RESEARCH ARTICLE
10.1029/2021JA029973

Key Points:

- We use hybrid simulations to explain the early formation of tangential discontinuity-driven foreshock bubbles and hot flow anomalies
- At discontinuities, foreshock ions perform partial gyrations and drive currents that determine the magnetic field profile of structures
- Discontinuity properties relative to the foreshock ion gyromotions account for the differences in the formation between the two structures

Supporting Information:

Supporting Information may be found in the online version of this article.

Correspondence to:

H. Zhang and T. Z. Liu,
hzhang14@alaska.edu;
terryliuzixu@ucla.edu

Citation:

Vu, A., Liu, T. Z., Zhang, H., & Delamere, P. (2022). Hybrid simulations of a tangential discontinuity-driven foreshock bubble formation in comparison with a hot flow anomaly formation. *Journal of Geophysical Research: Space Physics*, *127*, e2021JA029973. https://doi.org/10.1029/2021JA029973

Received 15 SEP 2021
Accepted 1 JUN 2022

Hybrid Simulations of a Tangential Discontinuity-Driven Foreshock Bubble Formation in Comparison With a Hot Flow Anomaly Formation

Andrew Vu[1], Terry Z. Liu[1,2,3], Hui Zhang[1], and Peter Delamere[1]

[1]Geophysical Institute, University of Alaska Fairbanks, Fairbanks, AK, USA, [2]Cooperative Programs for the Advancement of Earth System Science, University Corporation for Atmospheric Research, Boulder, CO, USA, [3]Department of Earth, Planetary, and Space Sciences, University of California, Los Angeles, CA, USA

Abstract Hot flow anomalies (HFAs) and foreshock bubbles (FBs) are significant foreshock transients that can accelerate particles and disturb the magnetosphere-ionosphere system. Yet, their early formation mechanisms are still not fully understood. To investigate the formation of tangential discontinuity (TD)-driven FBs and HFAs, we use 2-D local hybrid simulations where a reflected or an injected warm foreshock ion beam can interact with a TD whose half-thickness is comparable to the ion inertial scale. We show that the foreshock ions perform a partial gyration within, or across, the TD. Bulk motion differences between partially-gyrating foreshock ions and fluid-electrons lead to the generation of currents. As the trigger, these foreshock-driven currents change the magnetic field topology around the TD and force the frozen-in solar wind plasma to redistribute along with the field lines, shaping the foreshock transient. This confirms a recently proposed kinetic formation model. The extent of the magnetic field direction change across the TD within the foreshock ion gyromotion determines the current profile and thus the type of foreshock transient that forms. For a thin TD, the foreshock ions generate a current that is much stronger on the upstream side than the downstream side, forming an FB with one upstream compressional boundary. For the same foreshock ion gyroradius and magnetic shear, a thick TD yields comparable foreshock-driven currents on the upstream and downstream sides, forming an HFA with two compressional boundaries. Our study suggests that the TD thickness is one of the factors that determine the formation of FBs and HFAs.

1. Introduction

At the quasi-parallel bow shock, backstreaming ions populate the upstream region known as the foreshock (e.g., Eastwood et al., 2005). In the ion foreshock, interactions between these backstreaming foreshock ions with the solar wind ions (and discontinuities) lead to the observations of numerous transient kinetic phenomena (see review by Zhang et al., 2022), such as hot flow anomalies (HFAs) (Chu et al., 2017; Lucek et al., 2004; Paschmann et al., 1988; Schwartz, 1995; Schwartz et al., 1985, 2018; Thomsen et al., 1986; Wang et al., 2012; Zhao et al., 2015), spontaneous hot flow anomalies (Omidi et al., 2013; Zhang et al., 2013), foreshock bubbles (FBs) (Liu et al., 2015; Omidi et al., 2010, 2020; Turner et al., 2013, 2020), foreshock cavitons (Blanco-Cano et al., 2009, 2011; Kajdič et al., 2011), foreshock cavities (Billingham et al., 2008; Sibeck et al., 2002), and Short Large Amplitude Magnetic Structures (e.g., Schwartz et al., 1992). Two types of foreshock transients with very significant observational signatures, FBs and HFAs, exhibit greatly deflected plasma bulk flows and increased plasma temperatures within their low-density cores. HFAs usually expand slowly on two sides with spatial scales of 1–3 R_E (e.g., Facskó et al., 2009), whereas FBs typically expand super-magnetosonically only in the upstream direction, resulting in larger spatial scales (2–10 R_E) and a shock bounded only upstream of their cores (e.g., Liu, Turner et al., 2016; Turner et al., 2020). Because of the significant dynamic pressure disturbances within foreshock transient cores and the ambient solar wind, FBs and HFAs can deform the local bow shock surface and disturb the magnetosphere upon interaction (e.g., Archer et al., 2015, 2014; Hartinger et al., 2013; Jacobsen et al., 2009; Sibeck et al., 1999; Wang et al., 2020; Wang, Zhang, et al., 2021). In addition, FBs and HFAs can aid in the acceleration of particles at the bow shock (e.g., Liu, Angelopoulos, et al., 2017; Liu et al., 2018, 2019; Liu, Hietala et al., 2016; Liu, Lu, et al., 2017, 2020; Omidi et al., 2021; Turner et al., 2018; Wilson et al., 2016).

The formation mechanisms of FBs and HFAs and their intrinsic differences are not entirely understood. In hybrid simulations by Thomas et al. (1991), Lin (1997, 2002), and Omidi and Sibeck (2007), solar wind tangential

discontinuities (TDs) can concentrate and thermalize backstreaming particles as they convect along the bow shock surface. The backstreaming particles within this region of higher thermal pressure can expand outward into the ambient cold plasma, resulting in a low-density core bounded by compressional boundaries or shocks. In addition, hybrid simulations show that FBs can form with a rotational discontinuity (RD) (Omidi et al., 2010). However, spacecraft observations show FBs can also be driven by TDs (Liu et al., 2015), which is later confirmed by 3-D global hybrid simulations by Wang, Wang, et al. (2021). Archer et al. (2015) and Liu et al. (2015) explain the process by which foreshock ions gain thermal energy as they encounter the magnetic field change across a discontinuity; a portion of the foreshock ions' parallel speed becomes projected into the perpendicular direction, increasing the foreshock ions' thermal energy. The reduction in their parallel speeds also leads to the local accumulation of foreshock ions due to mass flux conservation. The enhancement in thermal energy and density together causes thermal pressure to increase, which leads to the formation and expansion of FBs and HFAs. However, the concept of thermal pressure is not valid for foreshock ions as foreshock ion gyroperiods (10–20 s) are comparable to the time scales of HFAs and FBs, and foreshock ion gyroradii (1000 s of km) are larger than or comparable to solar wind discontinuities. Therefore, it is imperative to treat foreshock ions as kinetic particles. In addition, this model does not explain the formation differences between TD-driven FBs and HFAs. As case studies by Liu, Turner, et al. (2016) show that, under almost the same solar wind conditions, a thin TD formed an FB, and a thick TD formed an HFA, suggesting that TD thickness may play a critical role in the formation process.

Recently, particle-in-cell (PIC) simulations by An et al. (2020) and Magnetosphere Multiscale spacecraft (MMS) observations by Liu, Lu, et al. (2020) demonstrate a physical formation model of FBs and HFAs involving the kinetic effects of foreshock ions. In their model, foreshock ions become demagnetized at the driver discontinuity as the electrons remain magnetized. This results in a Hall current that alters the magnetic fields around the discontinuity. The magnetic field variations induce an electric field that drives cold plasma $\mathbf{E} \times \mathbf{B}$ outward, together with the field lines, leading to an expansion of the structure. The foreshock ions performing a partial gyration against the induced electric field provide the energy necessary for the expansion. However, their PIC simulations only involved an RD and did not fully explore the formation differences between TD-driven FBs and HFAs.

In this paper, we will use local hybrid simulations to confirm the kinetic formation model of foreshock transients involving a discontinuity. We will show the differences in the early formation processes of TD-driven FBs and HFAs via two ways. First, by using a more realistic setup involving a moving TD interacting with a planar shock, and second, by using a simpler setup of a stationary TD interacting with an injected foreshock ion beam. Considering the kinetic effects of the foreshock ions, we will prove that when foreshock ions interact with a TD of comparable scale size, they lead to the generation of currents that change the magnetic field of the TD. And depending on the initial thickness of the TD, the resultant magnetic field changes dictate whether an FB or an HFA will form at the early stage. A TD-driven FB forms from a thin TD, and an HFA forms from a thick TD. We organize this paper as follows. We will first introduce the hybrid code, describe the initial simulation setups, and define the simulation parameters in our FB and HFA runs in Section 2. In Section 3, we will present the simulation results of both the planar shock and the injection of a foreshock ion beam, interacting with a thin (thick) TD to form an early stage TD-driven FB (HFA). In Section 4, we will discuss the importance of the TD thickness as one of the factors in determining whether an FB or HFA forms and describe the early formation process of the FB and HFA in the simulations. In Section 5, we conclude and mention future work using hybrid simulations.

2. Method

To understand the interactions between a foreshock ion population with a TD, we build a local 2-D hybrid simulation that uses kinetic ions and fluid electrons (Delamere, 2006, 2009; Delamere et al., 1999; Swift, 1995, 1996). The code assumes quasi-neutrality, is non-radiative, and has electrons being a massless and charge-neutralizing fluid. Ion particle motion for each cloud-in-cell macroparticle is determined by

$$\frac{d\mathbf{v}}{dt} = \mathbf{E} + \mathbf{v} \times \mathbf{B} - \nu\left(\mathbf{u}_\mathrm{i} - \mathbf{u}_\mathrm{e}\right),$$

where $\mathbf{E}$ is in units of ion acceleration, $\mathbf{B}$ is in units of gyrofrequency, ν is the collision frequency between ions and electrons. The electric field is calculated through a combination of the electron momentum equation and Ampere's law

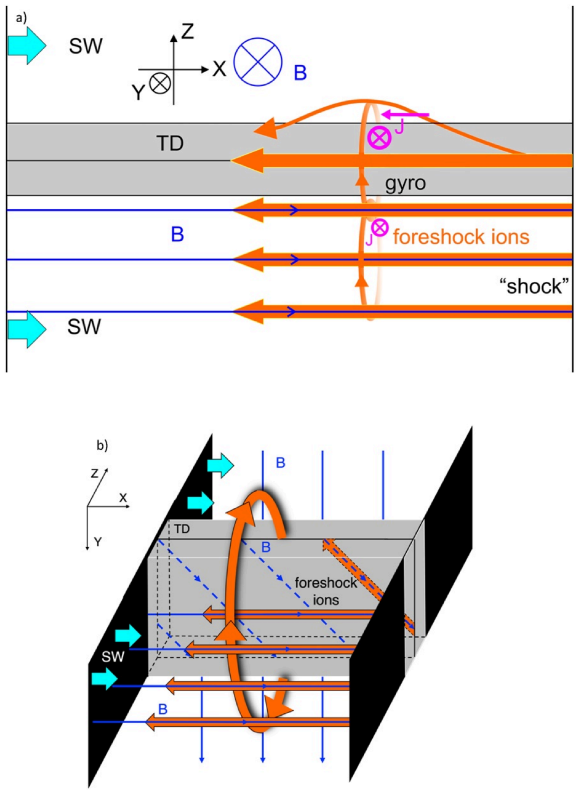

Figure 1. The setup of the simulation box in the 2-D local hybrid simulation in 2-D (3-D) in panel a (panel b). Solar wind ions are injected at the left boundary, and foreshock ions are either generated by the reflection of solar wind ions at the planar shock or injected at the right boundary. The magnetic field is directed to the right in the +x direction below (in front of) the tangential discontinuity (TD) and directed in the +y direction above (behind) the TD. The gray box represents the TD, with a normal along the +z direction, where the magnetic field change occurs. In panel a, the motion of foreshock ions (orange arrows) across the TD and at the bottom edge of the TD, into the +y and −x direction, leads to the generation of currents (magenta arrows). In panel b, the motion of foreshock ions (dashed orange arrows) within the TD is tilted.

$$\mathbf{E} = -\mathbf{u}_e \times \mathbf{B} - \nu(\mathbf{u}_e - \mathbf{u}_i) = -\left(\mathbf{u}_i - \frac{\nabla \times \mathbf{B}}{\alpha n}\right) \times \mathbf{B} - \nu \frac{\nabla \times \mathbf{B}}{\alpha n},$$

where $\alpha = \mu_0 q^2/m_p$ and m_p is the proton mass. The α parameter is used to scale the ion macro-particle densities to physical values. Faraday's law is used to advance the magnetic fields. Particle and field equations include dissipation terms for the ion-electron collisions to reduce numerical instabilities. Particle updates use a predictor-corrector scheme, and the fields are updated in sub-cycles of fractional particle time steps using the leap-frog technique.

In the simulation setup sketched in Figure 1, we orient the magnetic field to be in the +x direction (pointing to the right) in the bottom half and the +y direction (pointing into the page) in the top half. Encompassing the region where the field changes between the parallel shock (bottom) region and the perpendicular shock (top) region is the TD that follows the Harris current sheet model with a half-thickness that is comparable to the ion inertial length. In addition, because of the field strength dip at the center of the TD, we place additional ion macroparticles inside the TD to maintain a pressure balance. For the simulation box in Figure 1, we implement open boundary conditions where the particles and fields exit at the left and z (top and bottom) boundaries and periodic boundary conditions in the y direction (in and out of the page).

For the first test, we set the right-side boundary, opposite of the solar wind injection boundary, to reflect incoming solar wind ions to form a planar shock. With the formed shock, some of the solar wind particles are reflected in the quasi-parallel region, forming the foreshock. Then we launch a TD that propagates downward (−z) at a speed of 1.0 V_A along the planar shock surface. In these runs of a real planar shock, a thin TD and a thick TD formed an early-stage FB and HFA, respectively.

To further examine how the foreshock ions interact with the TD during the early formation stage of FBs and HFAs, we then use a simple injection model. In place of the planar shock, we continuously inject a constant warm foreshock ion beam at the right boundary that acts as a "shock," as seen in Figure 1, where the magnetic field is exactly parallel and quasi-parallel to the right boundary normal (i.e., we only inject foreshock ions on one side of the TD). In addition, the foreshock ion bulk speed is twice the solar wind ion bulk speed and directed against the solar wind and magnetic field direction (−x direction). Within the narrow quasi-parallel region (bottom half of the TD), the injected foreshock ions are initialized with an additional $\mathbf{E} \times \mathbf{B}$ component to remain field aligned. In this simple injection model, the solar wind ions do not become reflected, but leave the simulation domain when they encounter the right boundary.

To make sure that a substantial number of injected foreshock ions do not gyrate back out of the simulation box, we ensure that the parallel speeds of the foreshock ions are greater than the peak thermal speed from the Maxwellian distribution. The ratio of injected foreshock ions to solar wind ions is held constant throughout the parallel/quasi-parallel side of the TD. We use a high density of the injected foreshock ions (relative to the typical foreshock ion densities observed in the planar shock) to emphasize and study their kinetic effects (smaller foreshock ion densities do not affect the physical process but only make the resulting structure weaker).

For the solar wind ions in both the real planar shock model and the simple injection model, we initialize a background of and continuously inject, at the left ($x = 0$) boundary, a cold solar wind Maxwellian population with a bulk flow speed along the +x direction. Because of the magnetic field configuration, the convection electric field points toward the TD in the top half and ensures the formation of a TD-driven FB and HFA (e.g., Liu et al., 2015; Schwartz et al., 2000) (In the Supporting Information S1, we also show the case of B_y pointing in the opposite direction, which leads to the convection electric field pointing away from the TD and no HFA or FB forms).

Considering the kinetic effects of the foreshock ions, shown in the cartoon in Figure 1, the foreshock ions initially move along the field in the –x direction and when they cross the discontinuity, because of the relative scale sizes, they perform a partial gyration in the –y direction. This deviation in the bulk flow of the foreshock ions, with the fluid electrons, leads to the generation of a current that then changes the magnetic field of the TD. We will present evidence for the bulk motion of the foreshock ions and the generation of currents in this paper.

To examine whether the thickness of the discontinuity (relative to the foreshock ion gyroradius) determines the type of foreshock transient that forms, we perform two simulation runs in each real shock model and injection model, with different TD half-thicknesses, to compare their generated currents and structures. For the planar shock simulation runs, we use TD half-thicknesses of 20 solar wind ion gyroradii and 50 solar wind ion gyroradii for the thin and thick TDs, respectively. For the injection model, to highlight the role of the TD thickness, we use a much larger difference between the TD half-thicknesses. And so, we set the thin TD half-thickness to be 2 (0.25) solar wind (foreshock) ion gyroradii, and the thick TD half-thickness to be 32 (4) solar wind (foreshock) ion gyroradii. We keep all other simulation parameters constant between the two runs. The background magnetic field strength and solar wind density are set at 5.00 nT and 5.00 cm^{-3}, resulting in an Alfvénic speed of 48.95 km/s. The solar wind ion bulk flow speed is 10 M_A, and the foreshock ion bulk flow speed is 20 M_A (against the solar wind flow). The foreshock ion to solar wind ion density ratio is 0.12, and the foreshock ion gyroradii are 8 times that of the background solar wind ions. We use a simulation domain that is initialized with an ion plasma beta of 1.0, a simulation box of 202 × 802 cells where the dimension of each cell is 0.5 ion inertial lengths (or solar wind ion gyroradii, in this setup), 400 macroparticles per cell, and a macroparticle weighting of 1:50 between the solar wind ion and foreshock ion macroparticles.

3. Results

3.1. Foreshock Bubble Formation

To simulate a more realistic environment for the interaction between a TD and foreshock ions, we use a solar wind TD (with its center initialized at $z = 300$ gyroradii) that is thin (20 gyroradii) and propagating in the −z direction ($-1.0\ V_A$) interacting with a planar shock that is quasi-parallel below (cone angle of 5°) and quasi-perpendicular above (cone angle of 95°) the TD. From Figures 2.1a and 2.2a, there is a compressional boundary that forms slightly below the initialized TD position between $z = 280$ and 290 gyroradii. Below this z position is a core region with decreasing ion density (comparing between the two moments in Figure 2a), increasing ion temperature (Figure 2b), increasing foreshock ion density (Figure 2c), and increasing velocity deflection (Figures 2d and 2f). Similar to the total ion density profile, there are enhancements of the magnetic field components, B_x and B_y, followed by a core region of low field strengths (Figures 2.2g and 2.2h). Responsible for the change in the magnetic field components B_x and B_y, respectively, are the enhanced signatures of bipolar J_y and J_x current density components in Figures 2.2m and 2.2n. Downstream of the core region, there is no clear compressional boundary that develops. Therefore, the characteristics of the early-stage structure (see line plots in Figure S4 of the Supporting Information S1) are consistent with FB observations by Liu et al. (2015); Liu, Turner, et al. (2016) and global hybrid simulations by Wang, Wang et al. (2021).

From Figures 2h and 2i, there are foreshock ultra-low frequency (ULF) waves growing in the downstream background foreshock, which propagate in the x direction with periodic magnetic field changes in the transverse yz direction. Considering that there is a spatial separation between the FB and the ULF waves, our simulation results show that the ULF waves do not appear to play a role in the early development of the FB. And so, to control the properties of the foreshock ions interacting with the TD and to minimize the effects of the ambient fluctuations on our diagnosis of their interaction with the TD, we performed a simplified simulation model to pinpoint the origin of the currents (Figures 2m and 2n) that cause the significant magnetic field variations (Figures 2g and 2h). We change the simulation setup so that we inject a foreshock ion beam with a fixed thermal speed at the right boundary, in place of the reflecting boundary. We show the resulting simulation run below in Figure 3.

In this simpler injection model, the injected foreshock ions interact with a thin TD; the TD half-thickness is one-fourth of the injected foreshock ion gyroradius. Thus, the foreshock ions can easily gyrate across the TD, initiating the formation of an FB (see Movie S1 in the Supporting Information). Figure 3 shows the 2-D plasma and field properties of the FB formation at the earlier time (Figure 3.1) at $t = 3.00$ gyroperiods and a later time (Figure 3.2) at $t = 10.00$ gyroperiods. Between the earlier and later times of early formation, we see the continued

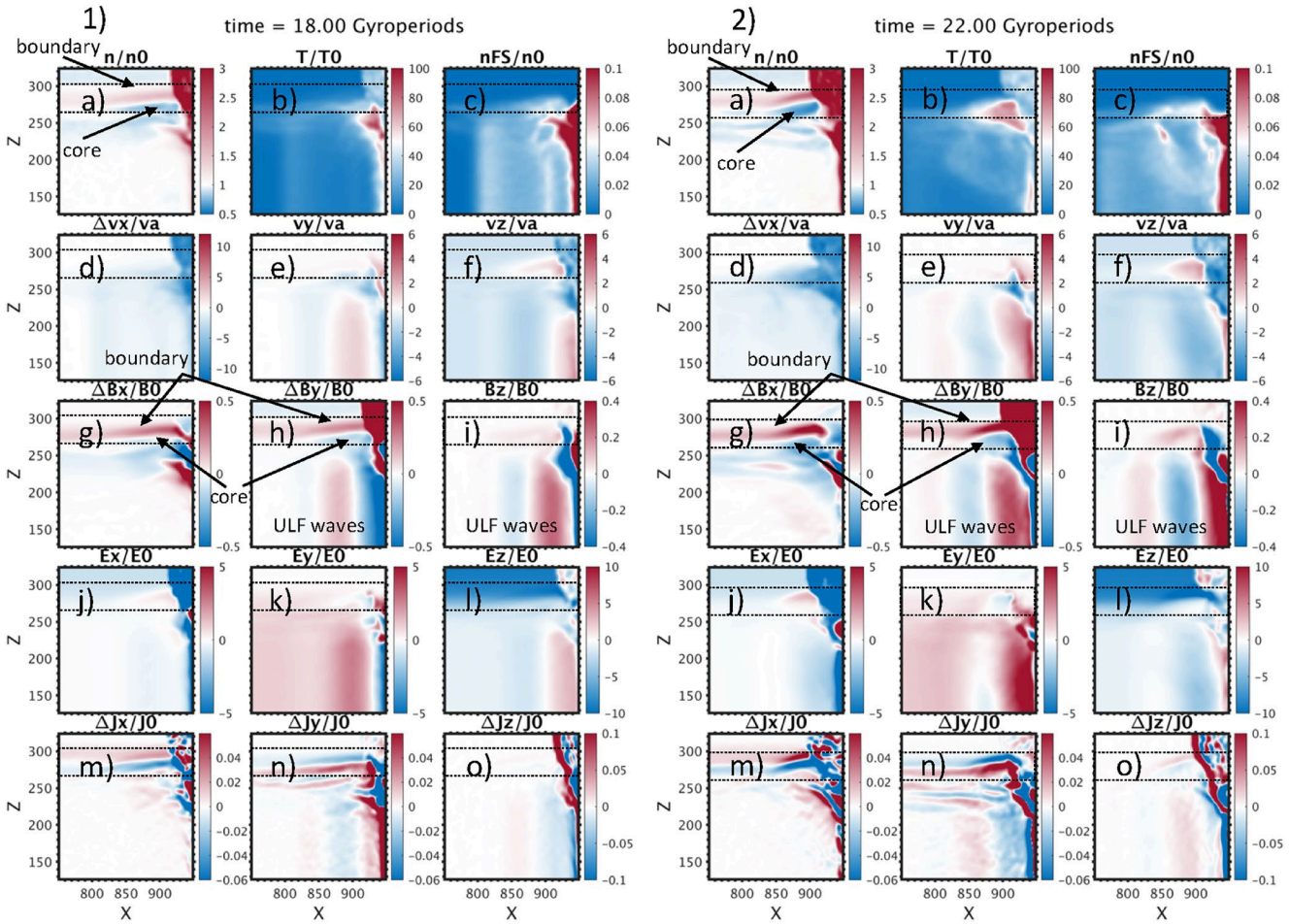

Figure 2. Panels (a–o) show the total ion densities, total ion temperatures, foreshock ion densities, ion bulk flow components, magnetic field components, electric field components, and current density components in the X-Z plane for a downward propagating thin tangential discontinuity (TD) interacting with a planar shock at an earlier time, $t = 18$ gyroperiods, (1) and later time, $t = 22$ gyroperiods, (2) of early formation. Panel (a) shows the total ion densities. Panel (d) shows the change in the ion bulk flow in the x direction and panel (f) shows the $-V_z$ motion of the solar wind and TD. Panels (g) and (h) show the change in the B_x and B_y components, respectively. Panels (m) and (n) show the change in the J_x and J_y components, respectively. The positions of the core, compressional boundary, and the ULF waves are marked. The horizontal dashed black lines are the z positions of the downstream (bottom) and upstream (top) edges of the TD. In panel c, the dark red (color saturated) region represents the ions that are moving in the −x direction but cannot escape the magnetosheath.

depletion of the ion density (Figure 3.2a) and magnetic field components (Figures 3.2d and 3.2e) at the core around the center of the TD ($z = 400$ gyroradii) and an enhancement of these quantities at the compressional boundary upside, or upstream, of the core. Accompanying the growth of the structure is the upward movement of the compressional boundary, initially between $z = 400$ and 410 gyroradii at the earlier time and then between $z = 410$ and 420 gyroradii at the later time. Quantitatively, by tracking the position of the peak density, the expansion speed of the compressional boundary is roughly 0.5 times the Alfvén Mach number against the solar wind in the simulation rest frame, resulting in a shock Alfvén Mach number of ∼1.4 in the shock normal incidence frame. The compressional boundary also increased its thickness along its normal direction. As there is only one compressional boundary and the whole structure forms dominantly in the quasi-perpendicular region (or the upstream side of the TD), the structure resembles that of a TD-driven FB consistent with Figure 2 and previous studies (Liu et al., 2015; Liu, Turner et al., 2016; Wang, Wang, et al., 2021). The overall size of the structure between $z = 400$ and 420 ion gyroradii corresponds to a physical distance of about 1,000 km, which agrees with the 1,000–2,000 km sizes of foreshock transients in their early formation observed by MMS (Liu, Lu, et al., 2020).

In Figure 3.2b, an increase in the foreshock ion density is responsible for the increase in the overall ion temperature (in addition to the solar wind ion heating) within the same region in Figure 3.2c. Examining the electric

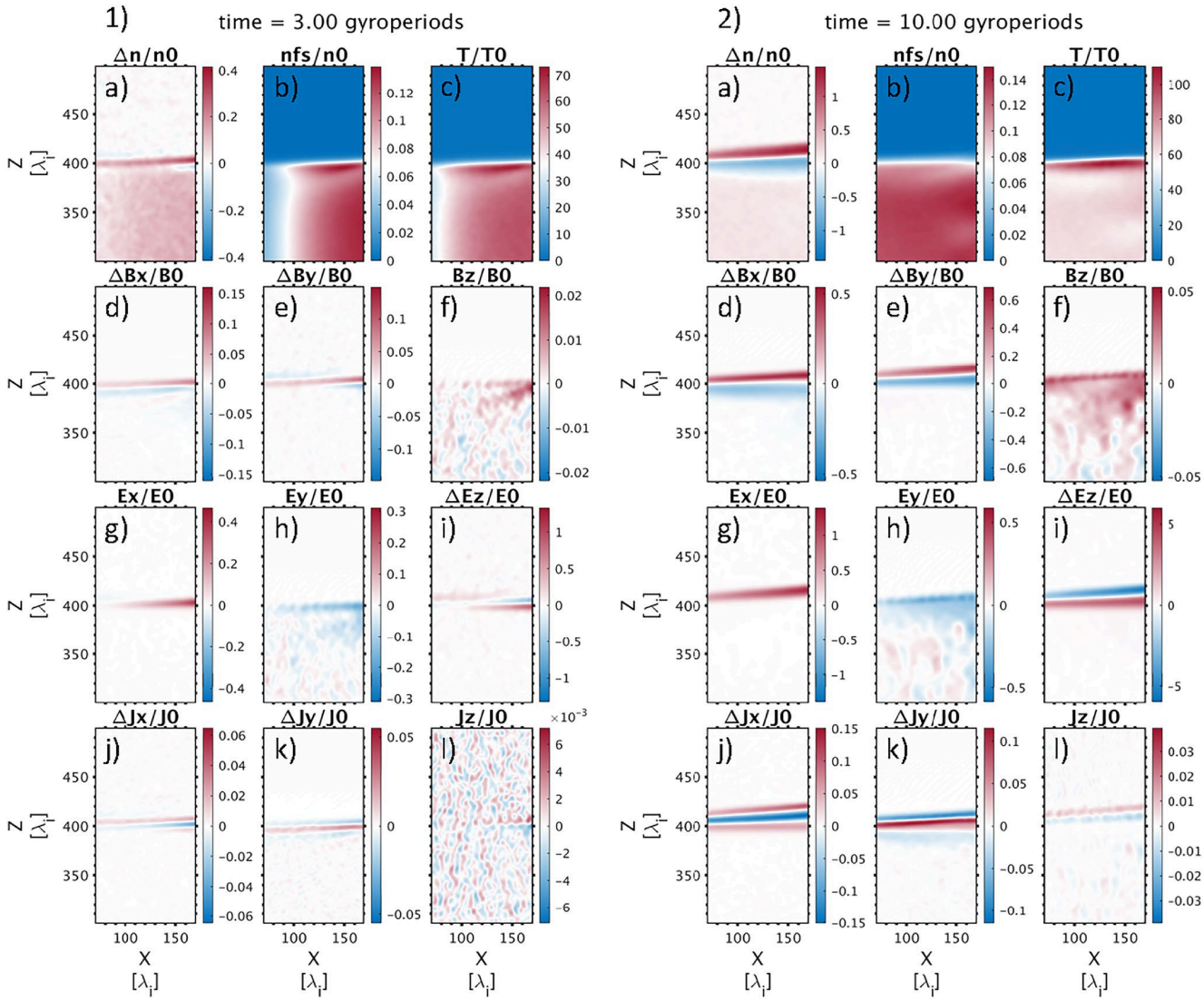

Figure 3. Panels (a–l) show the normalized total ion densities, foreshock ion densities, total temperatures, magnetic field components, electric field components, and current density components in the X-Z plane for an injected foreshock ion beam interacting with a thin tangential discontinuity at an earlier time, $t = 3$ gyroperiods, (1) and later time, $t = 10$ gyroperiods, of early formation (2). Panel (a) shows the change in the total ion densities. Panels (d and e) show the change in the B_x and B_y components, respectively. Panel (i) shows the change in the E_z component compared to the initial value. Panels (j and k) show the change in the J_x and J_y components, respectively.

fields, there is a positive E_x region within the compressional boundary in Figure 3.2g and a negative E_y region roughly corresponding to the FB core in Figure 3.2h. These are the induced electric fields that drive the cold plasma to $\mathbf{E} \times \mathbf{B}$ drift (expand) in the upward (+z) direction ($+E_xB_y$ and $-E_yB_x$) together with the field line transport. Figure 3.2i shows a negative ΔE_z (note that this is the variation of E_z compared to the initial value) above a positive ΔE_z, which is due to the B_y increase at the boundary ($-V_x\Delta B_y$) and the bulk velocity deflection in the x direction (ΔV_xB_y), respectively (see Figures 4a and 4c). In the PIC simulations by An et al. (2020), the major role of E_z in the solar wind rest frame is to exchange energy between the ions and electrons, which is ignored in the hybrid simulations.

As for the current density components, there is a significant change in ΔJ_x and ΔJ_y in panels *j* and *k*. In Figure 3.2j, there is a strong negative ΔJ_x bounded by two positive ΔJ_x. This ΔJ_x current configuration alters the magnetic field profile in ΔB_y to produce a bipolar signature, as seen in Figure 3.2e. Similarly, in Figure 3.2k, there is a strong positive ΔJ_y and negative ΔJ_y region on two sides that create a bipolar magnetic profile for ΔB_x in Figure 3.2d. Overall, these currents alter the initial field configuration provided by the TD by lowering B_x and B_y within the

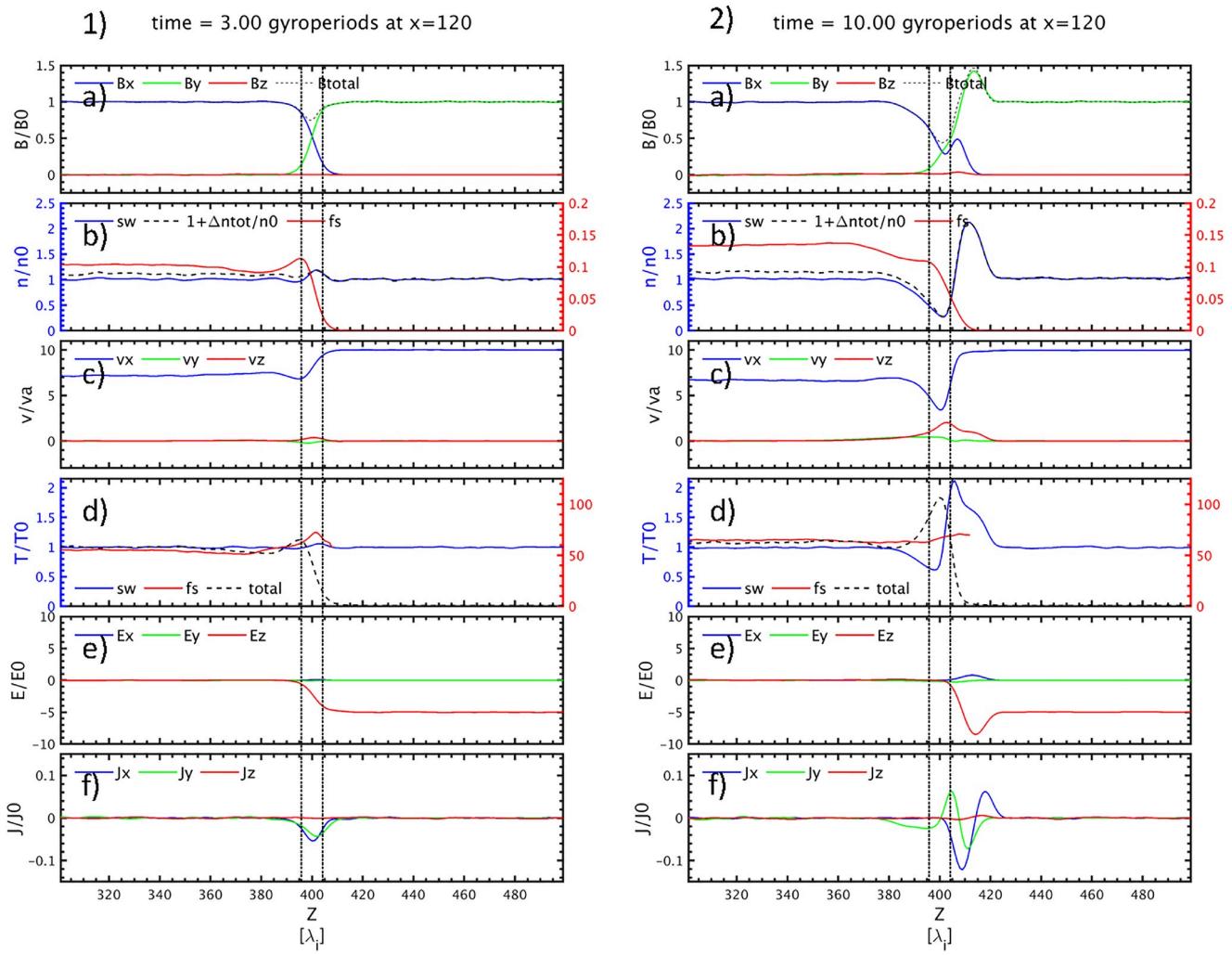

Figure 4. Panels (a–f) show the normalized magnetic field components, ion densities, ion bulk velocity components, ion temperatures, electric field components, and current density components along the z direction at $x = 120$ gyroradii for an injected foreshock ion beam interacting with a thin tangential discontinuity (TD) at an earlier time, $t = 3$ gyroperiods, (1) and a later time, $t = 10$ gyroperiods, (2) of early formation. In Panel (b), the blue (red) line shows the solar wind (foreshock) ion densities, and the dashed line shows the change in the total ion densities plus one. The vertical dotted lines show the initial extent of the TD thickness.

initial TD position and enhancing the field above the TD position. And because these currents grow in strength over time (between Figures 3.1 and 3.2), the magnetic field change also increases with time. These generated current density configurations from the injection method shown in Figures 3.2j and 3.2k are very similar to those from the planar shock method, shown in Figures 2.2m and 2.2n; therefore, our simplified injection model can indeed reproduce the appearances of the strong bipolar ΔJ_x and positive ΔJ_y current density components, which are key to the physics of the early formation process. We will show later that these currents are initially driven by the foreshock ion motions around the TD.

Taking a vertical slice of the 2-D panels at $x = 120$ gyroradii in Figure 3, we arrive at line plots of the magnetic field components, densities, ion bulk flow components, temperatures, and current components at the earlier (Figure 4.1) and later times of early formation (Figure 4.2). Note that, because of the dynamic growth of the structure, the scales between the two plots are different. These plasma and field properties resemble those of in-situ observations of an early FB formation (e.g., Liu, Lu, et al., 2020). Compared to the earlier time, the later time has an increased depletion of the magnetic field strength (panel a) from 0.75 B_0–0.40 B_0 and of the solar wind ion density (panel b) from 0.95 n_0 to 0.30 n_0. At the later time of early formation, there are more foreshock ions (red in panel b) that cross the center of the TD ($z = 400$ gyroradii). In addition, more foreshock ions penetrate further into the quasi-perpendicular side, away from the TD ($z > 400$ gyroradii), because of the magnetic field strength

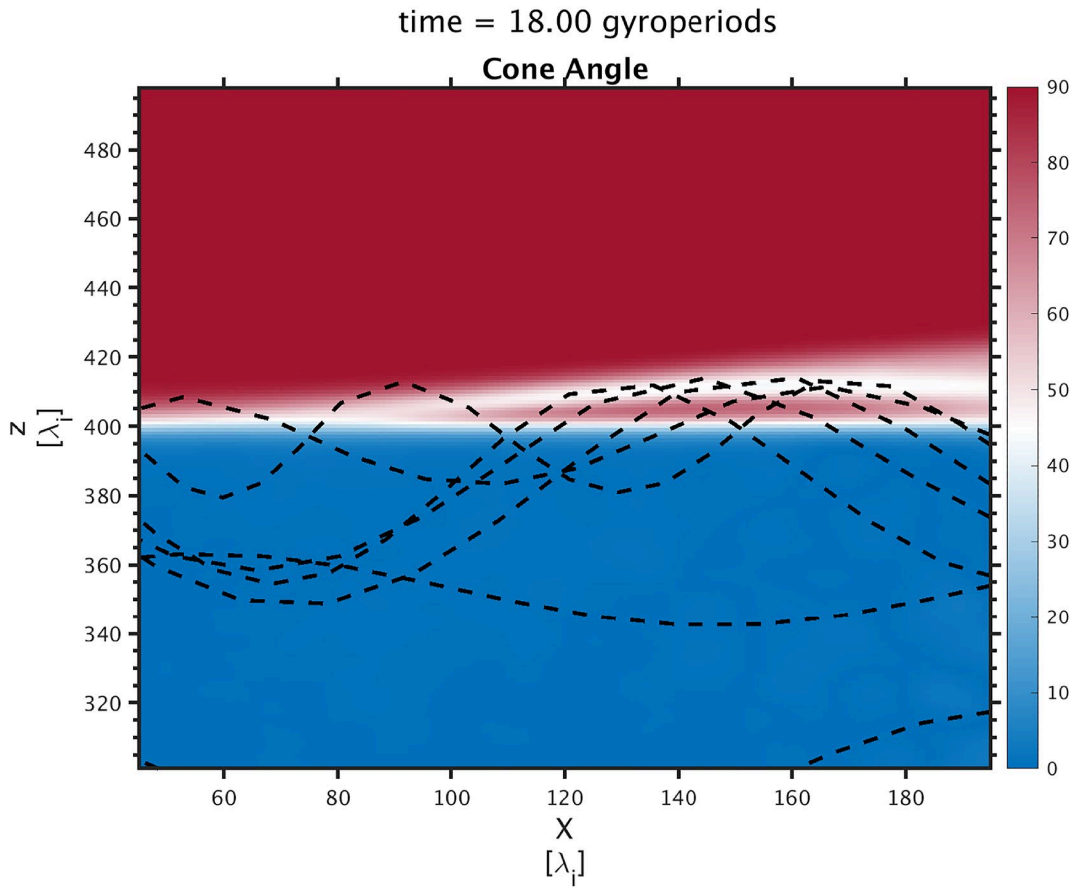

Figure 5. The cone angles between the magnetic field directions and the x-axis, and the trajectories of foreshock ions in the X-Z plane for an injected foreshock ion beam interacting with a thin tangential discontinuity (TD). The foreshock ions in this case can freely cross the center of the TD at $z = 400$ gyroradii.

decrease at the TD. There is also an increase in the solar wind ion density within the compressional boundary, whose peak position has shifted farther to the right, indicating that an expansion has taken place, from a 1.2 n_0 peak at $z = 402$ gyroradii to a 2.1 n_0 peak at $z = 411$ gyroradii. Panel c of the total ion bulk velocity components shows that the V_x component has significantly decreased from the ambient speed of 10 V_A to 3 V_A and that the V_z component has increased to 2 V_A within the core region of the FB. For the shock attached to the FB core, by the conservation of mass flux, we calculate its Mach number to be 2.03, with a sheath speed of 1.05 V_A (in the solar wind rest frame) and a density compression ratio of 2.07. Panel d shows a significant increase in the total ion temperature (dashed line) within the core region, because of the presence of foreshock ions within the core. There is also an increase in the solar wind ion temperature (blue line) at the compressional boundary as they become shocked and heated.

In Figure 4.1f, the current at the earlier time is dominated by the inherent current of the TD. At the later time of early formation, the current densities in Figure 4.2f show a bipolar signature in the J_x and J_y components from the core to the compressional boundary (between $z = 400$ and 425 gyroradii). Specifically, we see that the negative J_x increases in magnitude from -0.5 J_0 to -1.0 J_0, and the initial negative J_y becomes a positive J_y within the inner edge of the compressional boundary (between $z = 405$ to 410 gyroradii). These current variations are responsible for the changes to the magnetic field between Figures 4.1a and 4.2a.

To understand the origin of the current density variations, Figure 5 shows the foreshock ion trajectories across the center of the TD. The colors show the cone angles between the magnetic field and the x axis at a later time of early FB formation. We inject foreshock ions as a Maxwellian distribution with a foreshock ion gyroradius of about 16 cells, which is larger than the TD half-thickness of 4 cells; therefore, the foreshock ions can cross the TD center into the quasi-perpendicular or the ambient solar wind side. As the magnetic field rotates by 90° across the TD,

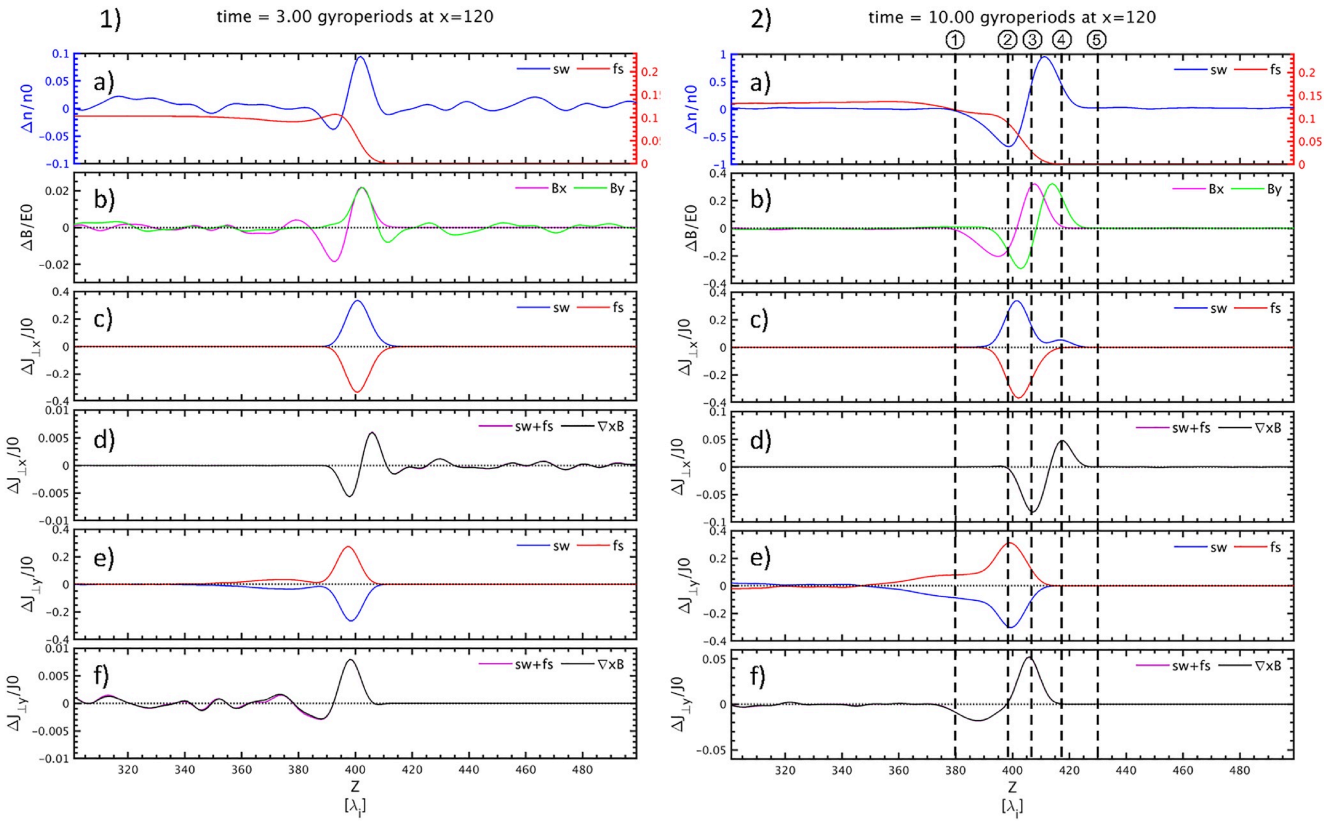

Figure 6. Panels (a–f) show the normalized change in ion densities, magnetic field components, solar wind current density, foreshock current density, and the current density from the curl of the magnetic field in the perpendicular x direction and perpendicular y direction relative to the magnetic field direction for an injected foreshock ion beam interacting with a thin tangential discontinuity at $x = 120$ gyroradii at an earlier time, $t = 3$ gyroperiods, (1) and a later time, $t = 10$ gyroperiods, (2) of early formation. In Panel (a), the blue line shows the total change in the solar wind ion densities, and the red line shows the foreshock ion densities. In Panels (c and e), the blue lines show the solar wind current density calculated by the difference in the bulk motions of the solar wind ions and electrons, $\mathbf{J}_{sw} = qn_{sw}(\mathbf{u}_{sw}-\mathbf{u}_e)$, and the red lines show the foreshock current density calculated by the difference in the bulk motions of the foreshock ions and electrons, $\mathbf{J}_{fs} = qn_{fs}(\mathbf{u}_{fs}-\mathbf{u}_e)$. In Panels (d and f), the purple lines show the total current density from the particle ions and fluid electrons, and the black lines show the current density from the curl of the magnetic field. The vertical dashed lines show the positions of the ion velocity distributions in Figure 7.

the crossing foreshock ions cannot immediately change their motion; therefore, the foreshock ions' initial parallel motion (−x direction) and gyromotion (+y direction on average) project to this new perpendicular field direction. The foreshock ions thus perform a partial gyration as they cross the center of the TD. With electrons being a magnetized fluid, the bulk motion differences between the crossing foreshock ions and fluid electrons result in a current that is directed mainly in the −x and +y directions (shown by the magenta arrow above the center of the TD in Figure 1a). In addition, as shown in Figure 5, the maximum extent of the foreshock ions that cross the center of the TD is roughly 16 cells in distance (this corresponds to the gyroradius of the warmest foreshock ions in the initialized Maxwellian distribution). This distance coincides with the farthest distance of the compressional boundary at this stage of the FB. The reason for this will be discussed later.

In Figure 6, we examine the drivers of the current density variations that produce the field variations associated with the FB. Here, we only focus on the perpendicular component and do not discuss the field-aligned currents for simplicity. In Figure 6.1a, we observe the Δn profile of the FB of a depleted core and a single compressional boundary. In Figure 6.1b, we already see the early development of a bipolar B_x variation and a positive B_y variation. Later in Figure 6.2b, the magnetic field variations grow 10-fold from 0.02 B_0 to over 0.2 B_0 in magnitude. We also see the bipolar ΔB_x signature shifts to the right from $z = 397$ to $z = 402$ gyroradii. In addition, the positive ΔB_y peak from before is now accompanied by a negative ΔB_y trough, forming a bipolar ΔB_y signature, and shifts to the right as well. Such evolution of field variations is caused by the growths of current density variations in the components $\Delta J_{\perp x}$ and $\Delta J_{\perp y}$ shown in panels d and f.

To pinpoint which of the ion populations is responsible for the generation of the current density variations, we plot the contribution to $\Delta J_{\perp x}$ (panel c) and $\Delta J_{\perp y}$ (panel e) from the motion differences between the solar wind ions and electrons (blue) and between the foreshock ions and electrons (red). In Figure 6.2c, the red line shows that the current variation, produced by the foreshock ions and electrons, is negative in the x direction between $z = 390$ and 410 gyroradii. This is the current produced by the foreshock ions' initial parallel motion (−x direction) projected to the perpendicular direction as they cross the TD (shown in Figure 5 and sketched in Figure 1). Conversely, the blue line shows that the current variation produced by the solar wind ions and electrons is positive in the x direction around the same positions. This is the response of the solar wind plasma to the field variations, which tends to resist such variation that is, this current variation (load) reduces the current from foreshock ions (driver) to revert the magnetic field variations back to their background values. Together, they result in a negative $\Delta J_{\perp x}$ in Figure 6.2d at the inner edge of the compressional boundary (within $z = 400$ to $z = 410$ gyroradii). This negative $\Delta J_{\perp x}$ decreases B_y in the core and increases B_y at the compressional boundary. The positive $\Delta J_{\perp x}$ at the outer edge of the compressional boundary (around $z = 420$ gyroradii), on the other hand, is driven by the solar wind plasma (blue in Figure 6.2c), which corresponds to the current at the shock surface and closes the current loop with the negative $\Delta J_{\perp x}$.

In the y direction, Figure 6.2e shows that the current variation produced by the foreshock ions and electrons (red line) is positive between $z = 390$ and 410 gyroradii. This is because when foreshock ions cross the TD, their initial gyromotion, which becomes a partial gyration, is in the +y direction on average (magenta arrow above the center of the TD in Figure 1a). Furthermore, the current variation by the solar wind ions and electrons (blue) is again opposite to the foreshock ion-driven current. Together, they result in a peak of positive $\Delta J_{\perp y}$ between $z = 400$ and 415 gyroradii (Figure 6.2f) that decreases B_x in the core and increases B_x at the compressional boundary. There is another negative $\Delta J_{\perp y}$, which closes the current loop with the positive $\Delta J_{\perp y}$, that reverts the magnetic field to the background value. Overall, the foreshock ions and electrons are the drivers of the generated currents, which decrease the field strength within the core and increase the field strength at the compressional boundary. The response of solar wind ions to such field variations tends to weaken the current driven by the foreshock ions and change the field back to the background value.

To further elaborate on the generation of currents by the foreshock ions, ion velocity distributions in Figure 7 show the behavior of the foreshock ions around the TD. Each column of the velocity distributions (columns 1–6) represents a z position corresponding to a vertical dashed line in Figure 6.2. The arrows in each of the panels show the projections of the +x (blue) and +y (red) directions in the panels' respective planes. In the first three columns of Figure 7, we see the solar wind ion distributions and the much warmer foreshock ion distributions. At position 1, panel a of the **B** versus **E** × **B** plane shows foreshock ions moving in the negative B direction, and panel f of the perp-perp (**B** × (**E** × **B**) versus **E** × **B**) shows foreshock ions as gyrotropic. This represents the typical foreshock ion distributions in the background foreshock. At position two inside the TD, we see the foreshock ion distributions become less gyrotropic in panel g, and at position three on the other side of the TD, a portion of foreshock ions cross the TD and gyrate partially (panel h). This is consistent with the above explanation that a portion of the initial motion of foreshock ions is projected to the new perpendicular direction as they cross the TD and enter the upstream region. Likewise, a portion of their initial motion also becomes the new parallel speeds. (As a result, 3-D global hybrid simulations by Wang, Wang, et al. (2021) show the entire FB being shifted along the magnetic field direction with time.) The bulk flow differences between the electron fluid and foreshock ion particles in the perpendicular plane projected to the −x and +y direction (panel h) create the currents shown in Figures 6c and 6e, consistent with Figure 5 and the sketch in Figure 1. At position 4, there are almost no foreshock ions, and the current in Figure 6 is driven by the solar wind ion particles and electron fluid. But because of the high density, the motion differences between the solar wind ions and electrons are not discernible in Figures 7d and 7i.

3.2. Hot Flow Anomaly Formation

This time, we study the interaction between a thick TD and a planar shock. Same as before in Figures 2 and 8 shows a solar wind TD, initialized at $z = 300$ gyroradii, that moves at a speed of $-1.0\ V_A$ downward, but now, the TD has a thickness of 50 gyroradii. At the earlier time in Figure 8.1a, there is a compressional boundary that forms below the initialized TD position at $z = 270$ gyroradii and another compressional boundary that appears near $z = 240$ gyroradii right above the bottom edge of the TD. Between these two compressional boundaries is a

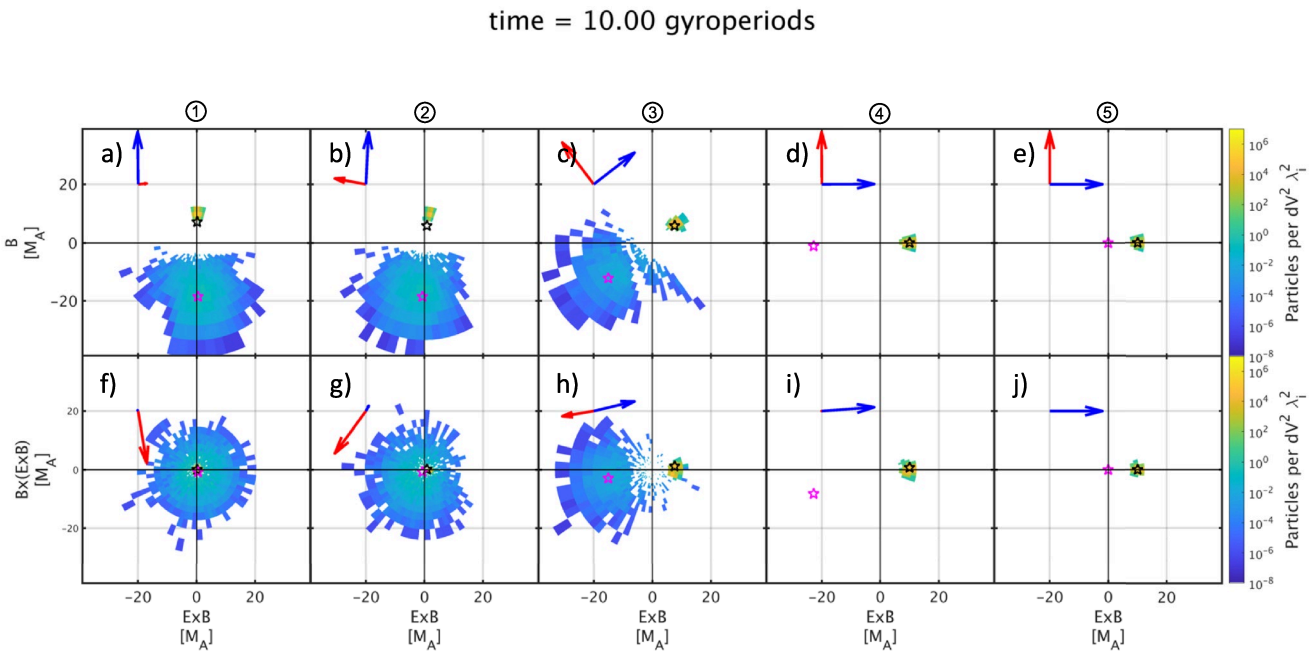

Figure 7. Panels (a–j) show the ion velocity distributions at $x = 120$ gyroradii and from the z positions indicated by the vertical dotted lines in Figure 6.2 for an injected foreshock ion beam interacting with a thin tangential discontinuity at a later time of early formation. The axes of Panels (a–e) are **B** versus **E** × **B**, and the axes of Panels (f–j) are **B** × (**E** × **B**) versus **E** × **B**. The blue arrow in each panel represents the projection +x direction in each plane, and the red arrow in each panel represents the projection of the +y direction (in-the-plane direction for the 2-D panels in Figure 3) in each plane. The black star represents the electron bulk flow, and the magenta star represents the foreshock ion bulk flow in the coordinate plane.

low-density core with enhanced ion temperature, foreshock ion density, and velocity deflection (Figures 8a–8f). The magnetic field variation is similar to the density variation in that there is a depletion and enhancements on two sides (Figures 8g and 8h). In addition, there is the development of two sets of bipolar J_x and J_y current density components that cause the magnetic field variations in B_y and B_x, respectively. Overall, these signatures (see line plots in Figure S5 of the Supporting Information S1) resemble those of an HFA with two compressional boundaries.

In the downstream background foreshock, there is the growth of ULF waves (Figures 8h and 8i). At the earlier time of $t = 16$ gyroperiods, there is a spatial separation between the formed HFA and the ULF waves (although at the later time of $t = 23$ gyroperiods, the ULF waves appear inside the HFA). In addition, the field strength enhancement of the HFA's downstream boundary is largely due to an increase of B_x (Figures 8.1g and 8.2g) because the downstream background magnetic field is mainly in the x direction. The field fluctuations by the ULF waves, on the other hand, are mostly in the transverse yz direction, and thus do not contribute to the field strength enhancement at the HFA's downstream boundary. Therefore, we believe that the early formation of the HFA boundaries is not related to the ULF waves (but later, as the ULF waves grow to be much stronger, they begin to play a role in shaping the downstream boundary). As before with the thin TD case, we proceed by using another simulation setup where there is an injection of a foreshock ion beam with a fixed thermal speed that interacts with a thick TD. In doing so, we hope to understand the reason for the current density configurations that cause the appearance of the second compressional boundary of the early stage HFA. We show the results of the simulation setup in Figure 9.

We now present the simulation results for the injection of foreshock ions that interact with a thick TD; the TD half-thickness is now four times the foreshock ion gyroradius. This presents a case where the foreshock ions cannot cross the entirety of the TD and reach the quasi-perpendicular region. In this setup, a structure forms that resembles an HFA with two compressional boundaries bounding a core (see Movie S2 in the Supporting Information). Figure 9 shows the 2-D plasma and field properties during the early formation at an earlier time (Figure 9.1), $t = 9.50$ gyroperiods, and later time (Figure 9.2), $t = 16.00$ gyroperiods. Between the earlier and later times of early formation, we see the growth of an additional compressional boundary at the downward side

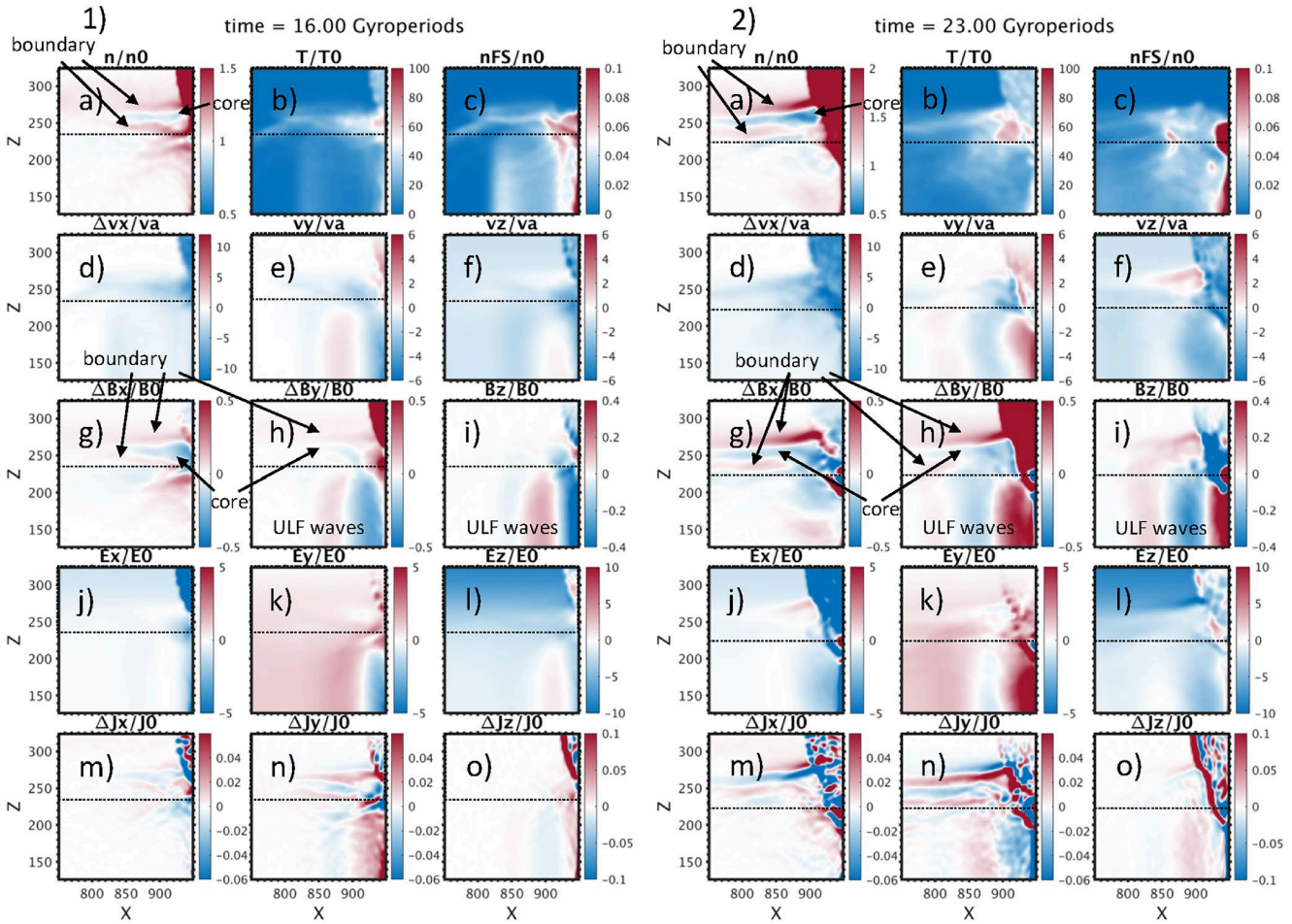

Figure 8. Panels (a–o) follow the same format as Figure 2 except for a downward propagating thick tangential discontinuity (TD) interacting with a planar shock at an earlier time, $t = 16$ gyroperiods, (1) and a later time, $t = 23$ gyroperiods, (2) of early formation. The horizontal dashed black line is the z position of the downstream (bottom) edge of the TD, and the upstream (top) edge of the TD is outside of the panel box at $z = 339$ gyroradii.

of the core near $z = 350$ gyroradii by the ion density enhancement in Figure 9.2a and the magnetic field enhancements in Figures 9.2d and 9.2e. There is also a further depletion of these quantities in the core region between $z = 380$ and 410 gyroradii. We also see that the size of the core region increases in the z direction on two sides, indicating that an expansion has taken place. In Figures 9.2j and 9.2k, the profile of ΔJ_x and ΔJ_y resembles the FB case (Figure 3), but there is one critical difference: in addition to $-\Delta J_x$ ($+\Delta J_y$) bounded by $+\Delta J_x$ ($-\Delta J_y$) on two sides, there is an additional $-\Delta J_x$ ($+\Delta J_y$) farther downward at $z = 300$ to 350 gyroradii. This additional current variation is responsible for the appearance of the additional compressional boundary compared to the FB case. Qualitatively, the appearances during the early formation of the two compressional boundaries in the densities and field components and the generated current density profiles responsible for the magnetic field variations at the TD are similar between the simulation setups of an injection of foreshock ions (Figure 9.2) and of a planar shock (Figure 8.1). Therefore, the simple model using the injection of foreshock ions is appropriate and captures the major physics in the early formation of the HFA.

The vertical slice at $x = 120$ gyroradii of Figure 9 provides line plots of the plasma and field properties for the HFA at the earlier (Figure 10.1) and later times (Figure 10.2) of early formation. Between the earlier and later times, there is an increased depletion within the core ($z = 385$ gyroradii) with the total magnetic field strength (panel a) from 0.75 B_0–0.6 B_0 and the solar wind ion densities (panel b) from 1.0 n_0 to 0.8 n_0. Around $z = 350$ and $z = 420$ gyroradii, there are the developments of two compressional boundaries on both sides of a core that show a slight ion flow deflection (panel c) and a slight ion temperature increase (dashed line panel d). The whole structure forms in the quasi-parallel side or the foreshock side of the TD. Thus, this structure, in contrast to the

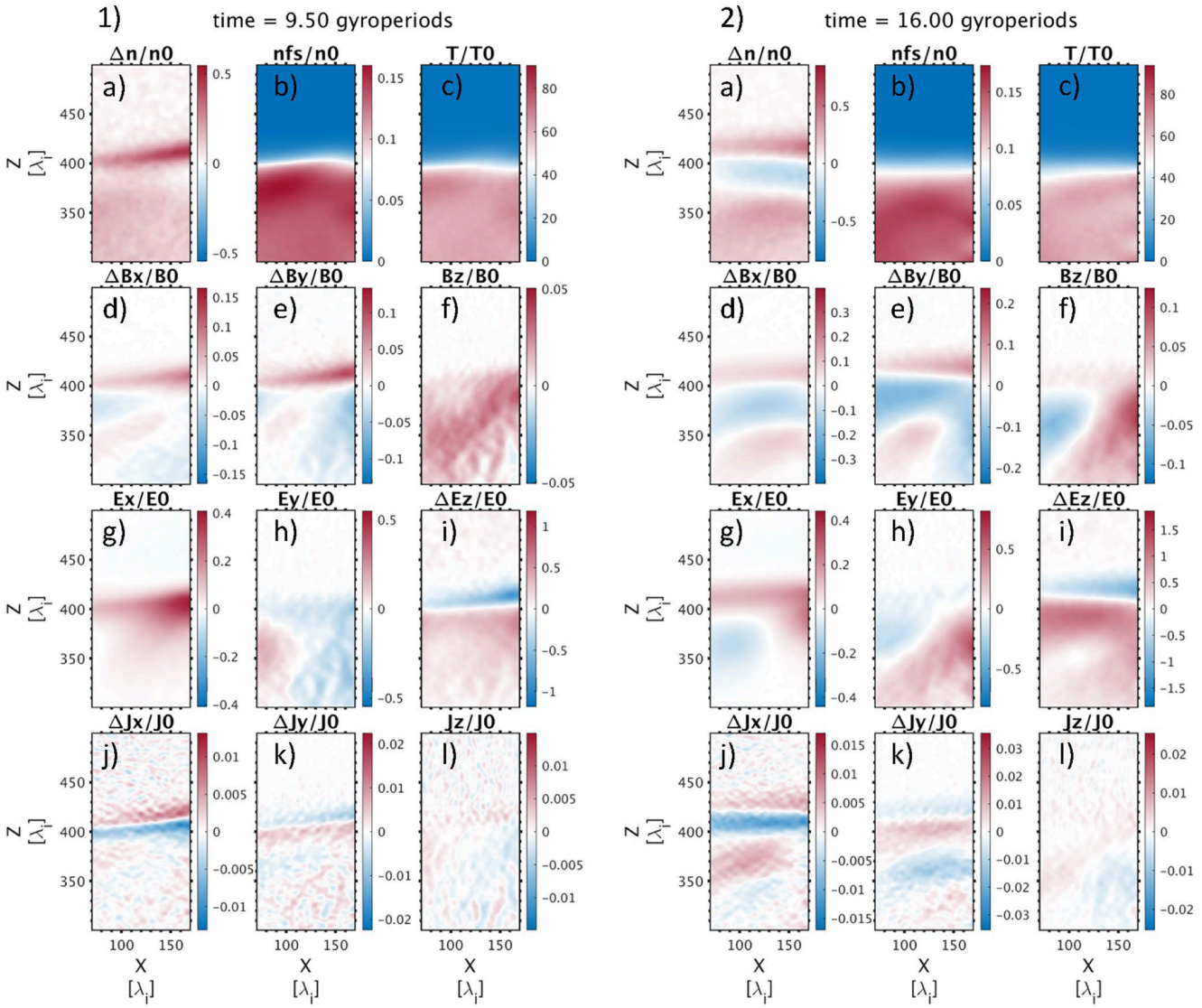

Figure 9. Panels (a–l) follow the same format as Figure 3 except for an injected foreshock ion beam interacting with a thick tangential discontinuity at an earlier time, $t = 9.5$ gyroperiods, (1) and a later time, $t = 16$ gyroperiods, (2) of early formation.

first run, resembles an HFA. There is also a TD directed electric field (E_z) on the upstream side of the TD (panel f) that is typically observed in HFA observations. Lastly, the plasma and field signatures within the HFA core, namely the magnetic field strength, ion density, ion flow deflection, and ion temperature, are much less significant than those from the FB core.

We show the trajectories of the foreshock ions within the TD in Figure 11. In this simulation case, the foreshock ions cannot fully cross the TD. For foreshock ions that cross the center of the TD, they produce currents similar to those in the FB case (magenta arrow above the center of the TD in Figure 1a). But because of the large TD thickness, the magnetic field change that the foreshock ions feel during their gyration is insubstantial. Therefore, there is a smaller portion of the foreshock ions' velocity projection that becomes a partial gyration when compared to the FB case, resulting in a weaker current. The weaker foreshock ion-driven currents then bring about weaker magnetic field variations within the TD and subsequently less significant signatures within the core of the HFA, compared to those within the core of the FB. In addition, the foreshock ions that do not cross the center of the TD can also generate currents because foreshock ions from different guiding centers, at different z positions, provide different gyrations and velocity projections because of the spatial variations in the field along the z direction within the TD (magenta arrow below the center of the TD in Figure 1a).

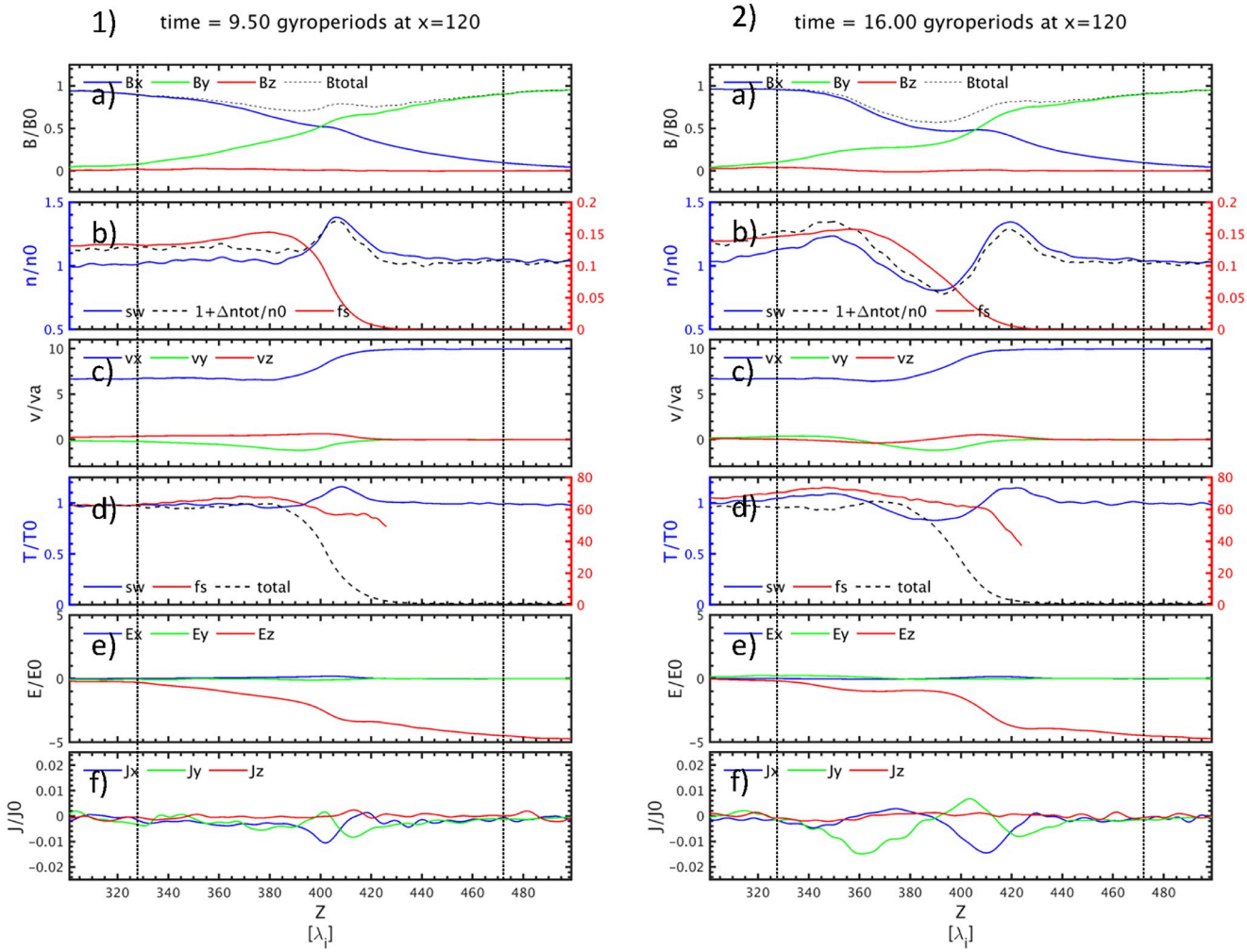

Figure 10. Panels (a–e) follow the same format as Figure 4 except for an injected foreshock ion beam interacting with a thick tangential discontinuity at an earlier time, $t = 9.5$ gyroperiods, (1) and a later time, $t = 16$ gyroperiods, (2) of early formation.

As expected, in Figures 12c and 12e, we see that the current density from the foreshock ions that cross the TD center (z positions roughly above 400 gyroradii) is only about 1/10 of the FB case (Figure 6). At the leading edge of the HFA (at $z = 315$ gyroradii in Figure 12f) there is $a\ +\Delta J_{\perp y}$ which is the net effect of foreshock ions with different gyrations inside and outside of the TD (we do not see a $-\Delta J_{\perp x}$ at this position because ΔJ_x is in the parallel direction). This $+\Delta J_{\perp y}$ is comparable to the $+\Delta J_{\perp y}$ caused by foreshock ions that cross the TD center (at $z = 410$ gyroradii in Figure 12f). As a result, these two $+\Delta J_{\perp y}$ together with the $-\Delta J_{\perp y}$ at $z = 360$ gyroradii (from the response of the solar wind plasma) lead to the two B_x enhancements on both sides of the B_x depletion. The B_x variations on the two sides induce electric fields of $-E_y$ and $+E_y$ (Figure 9h) that drive the solar wind plasma to $\mathbf{E} \times \mathbf{B}$ drift outward in both the +z and −z directions, leading to the density enhancements on the two sides (Figure 12a).

In Figure 13, we present the ion velocity distributions within the thick TD. Within the TD, because of their non-gyrotropy, the foreshock ion bulk motion shows a slight deviation from the electron bulk motion ($\mathbf{E} \times \mathbf{B}$ motion) at positions 1–3 that is projected mainly in the +y and slightly in the −x direction, consistent with Figures 12c and 12e. The motions of foreshock ions that cross the TD center (positions 4 and 5) exhibit a larger deviation from the motions of electrons than positions 1–3, but smaller compared to the FB case because of the smaller magnetic field direction change per gyroradius. In all, the smaller differences between the foreshock ion and electron bulk motions at the upstream boundary (positions 4 and 5), relative to in the FB case, account for the weaker foreshock ion-driven current and compressional boundary upstream. However, in doing so, the

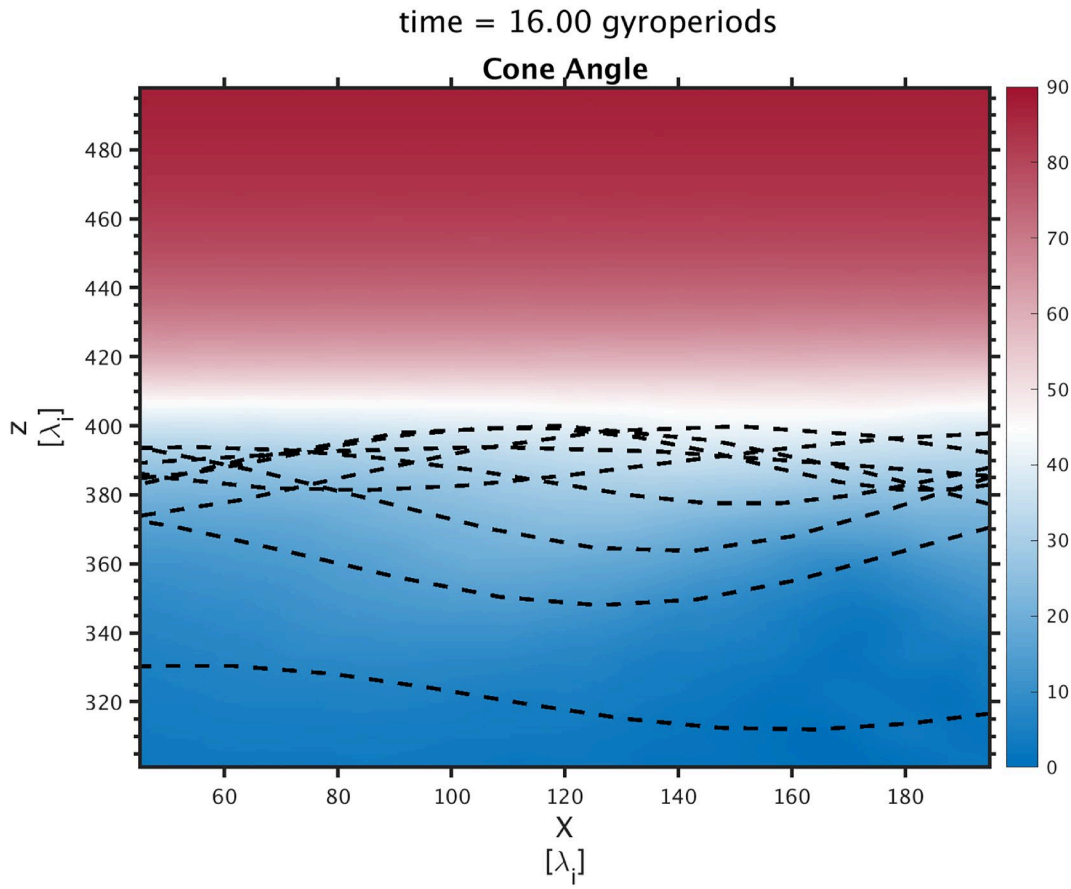

Figure 11. The cone angles between the magnetic field directions and the x-axis, and the trajectories of foreshock ions in the X-Z plane for an injected foreshock ion beam interacting with a thick tangential discontinuity (TD). The foreshock ions cannot fully cross the thick TD return to the quasi-parallel region when they encounter the initial TD center at $z = 400$ gyroradii.

upstream boundary then becomes comparable to the boundary formed at the downstream side, thus a structure resembling an HFA forms.

4. Discussion

Considering the kinetic effects of the foreshock ions at the TD that lead to the generation of currents that change the magnetic field of the TD, the goal is to show that for the same TD magnetic shear and foreshock ion gyroradius, the thickness of the TD determines whether the foreshock ion-driven currents will trigger the formation of an FB or an HFA. From the simulation runs involving a moving TD interacting with a planar shock, we find that, at the early stage, when the TD is thin, an FB forms, and when the TD is thick, an HFA forms. We also reach the same conclusion when we use an injection of a foreshock ion beam instead of a planar shock, judging by the ion density profiles, magnetic field variations, and current density configurations. Therefore, it is safe to replace the planar shock with an injection of a foreshock ion beam so that we can control the foreshock ion properties and minimize the growth of background ULF fluctuations. This allows us to more clearly diagnose the current density configurations that result in the observed magnetic field variations.

From the simulation runs using an injection of foreshock ions with a thin and thick TD, it is clear that the partial-gyrating motion of foreshock ions around a TD can act as the trigger and drive the early formation of an FB or HFA. One main difference in the observational characteristics between TD-driven FBs and HFAs is that FBs only expand in the upstream direction and do not form a compressional boundary on their downstream side. Our simulations provide an explanation for this distinction. In the FB case, the driver current is dominated by the

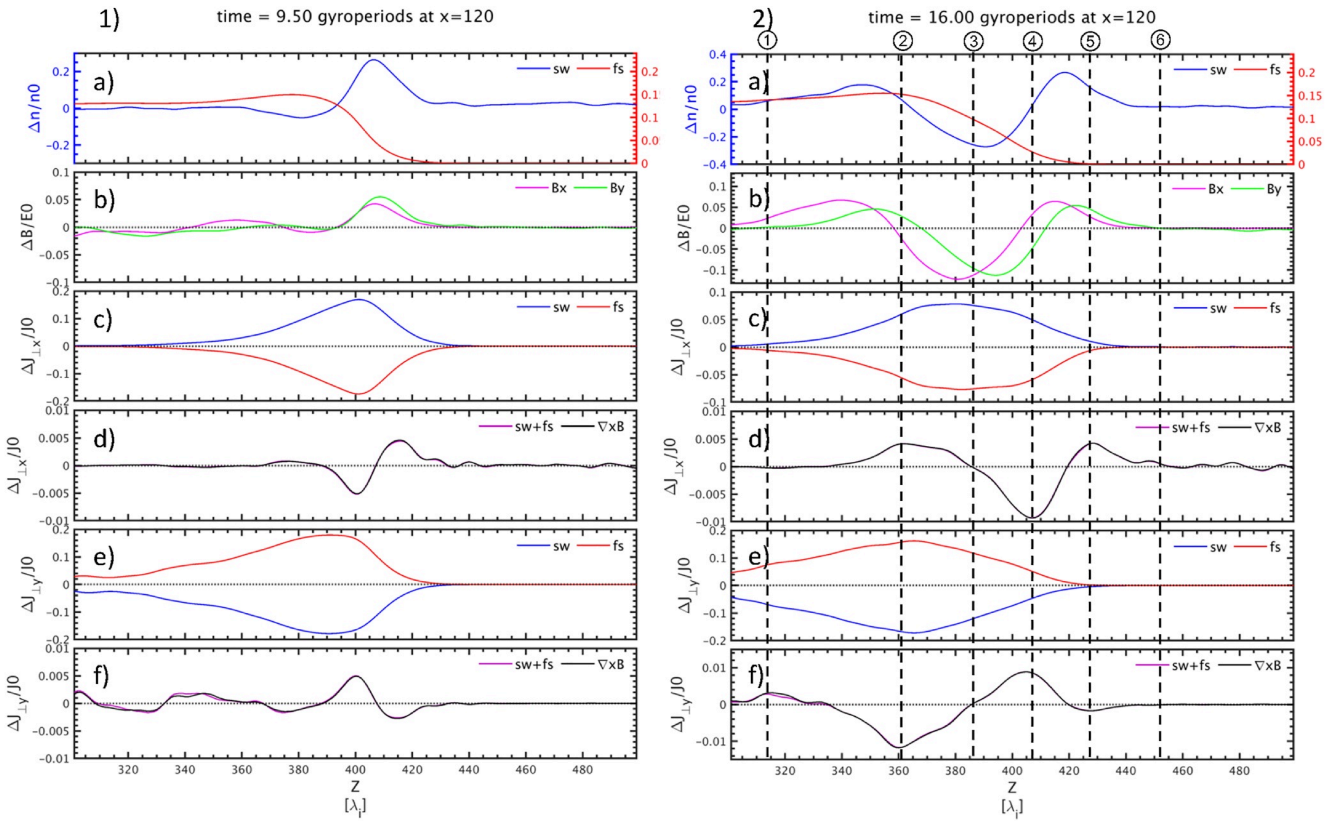

Figure 12. Panels (a–f) follow the same format as Figure 6 except for an injected foreshock ion beam interacting with a thick tangential discontinuity at an earlier time, $t = 9.5$ gyroperiods, (1) and a later time, $t = 16$ gyroperiods, (2) of early formation. The vertical dashed lines show the positions of the ion velocity distributions in Figure 13.

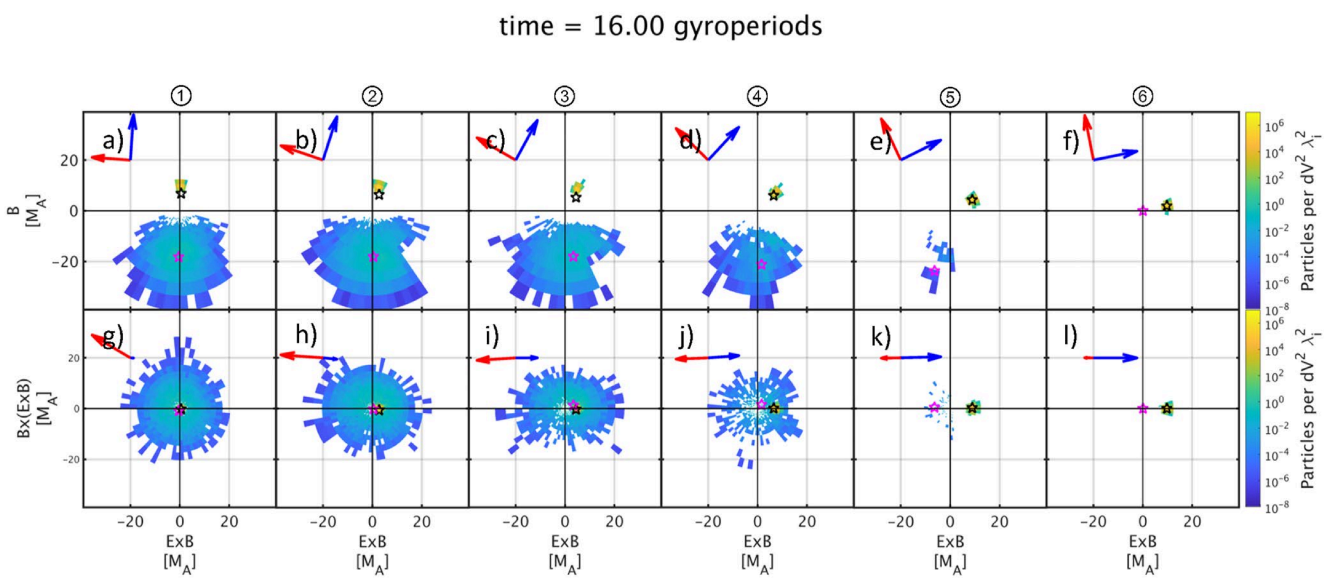

Figure 13. Panels (a–l) show the ion velocity distributions at $x = 120$ gyroradii and from the z positions indicated by the vertical dotted lines in Figure 12.2 for an injected foreshock ion beam interacting with a thick tangential discontinuity at a later time of early formation. The axes of Panels (a–f) are **B** versus **E** × **B**, and the axes of Panels (g–l) are **B** × (**E** × **B**) versus **E** × **B**. The blue arrow in each panel represents the projection +x direction in each plane, and the red arrow in each panel represents the projection of the +y direction (in-the-plane direction for the 2-D panels in Figure 9) in each plane. The black star represents the electron bulk flow, and the magenta star represents the foreshock ion bulk flow in the coordinate plane.

current from foreshock ions that cross the TD on the upstream side, and the net current around the downstream edge of the TD is relatively negligible (we can only observe it during the earlier time in Figure 6f at $z = 370$ gyroradii when the upstream current has not grown very strong). Thus, the field variation largely occurs on the upstream side and the corresponding induced electric field drives solar wind plasma to $\mathbf{E} \times \mathbf{B}$ drift (expand) mainly in the upstream direction. In the HFA case, on the other hand, the net upstream current, because of the foreshock ions partially gyrating near the center of the TD, is weak compared to the FB case. Even after the growth, the upstream current is still comparable to the current at the downstream edge of the TD. As a result, both sides have comparable field variations, and the corresponding induced electric fields can drive expansion in both directions.

From previous models, it is commonly believed that the enhancement of foreshock ion thermal energies causes the expansions of these structures. However, the projection of the perpendicular speeds does not increase the temperature, but rather, causes a partial gyration or bulk flow of the foreshock ions. In our simulations using an injection of foreshock ions, the foreshock ion temperatures relative to the bulk flow show little change. Therefore, it is not the thermal pressure, but the process described above that causes the early formation and expansion.

In addition, the expansion speed of the structure depends on the strength of the induced electric field, which is determined by how fast the magnetic field variations occur and how strong the foreshock ion-driven currents become. The strong foreshock ion-driven current in the FB case can also explain why FBs typically expand faster than HFAs to form a shock (e.g., Liu, Turner et al., 2016). Another point to consider is that a larger current from foreshock ions also means a greater energy conversion from the foreshock ions to the solar wind plasma (through the foreshock and solar wind current against and along the induced electric field, respectively) for expansion. In our simulation, the peak energy output, $\mathbf{J}\cdot\mathbf{E}$ of the foreshock ions in the FB case is roughly $-0.8\ J_0E_0$ whereas in the HFA case is roughly $-0.2\ J_0E_0$, a 4-fold difference.

In our simulations, where the magnetic shears across the TD and foreshock ion gyroradii are held constant, the different thicknesses of the TD are the only reason for the observed differences in the current strengths. To reiterate the process, as the foreshock ions gyrate within the field change of a TD, a portion of their parallel speed and gyrospeed is projected into the new upstream (above the TD) perpendicular direction. The foreshock ions, therefore, cannot complete their full gyromotion and can only perform a partial gyration around the TD. The velocity projection across the TD determines the strength of the current, which is controlled by the magnetic field direction change within one foreshock ion gyroradius. For the same magnetic shear angle, a thinner TD can cause a larger field direction change within one foreshock ion gyroradius. In general, with a thinner TD or a larger magnetic shear angle, the foreshock ions can perform more drastic partial gyrations and generate a stronger current. This could explain why in Liu, Turner, et al. (2016), a thick TD forms an HFA, and a thin TD forms an FB during the same time interval, and why a larger magnetic shear angle favors the formation of HFAs (e.g., Liu et al., 2021; Schwartz et al., 2000; Zhao et al., 2017).

In addition, we initially choose the simulation setup with a positive y directed magnetic field in the top half region to ensure the formation of the TD-driven FB and HFA (in this case, the convection electric field points toward the TD). This configuration allows for the foreshock ion-driven current to decrease the magnetic field strength within the TD, therefore initiating the positive feedback loop or instability introduced above. In the reverse scenario where the magnetic field is in the negative y direction in the top half region (the convection electric field points away from the TD), the foreshock ion-driven current reinforces the magnetic field strength within the TD (as shown in Figures S1, S2, and S3 of Supporting Information S1). This would not result in the formation of an FB or HFA, but rather a structure that has increased magnetic field strength and solar wind density within the TD.

Lastly, we discuss the role of the shock itself. Early in these simulation runs, the planar shock provides foreshock ions of sufficient density that go on to interact with the moving TD to generate the FB and HFA. We find that the initial gyrophase of the reflected solar wind ions is also important, as there was a delayed start for the FB formation as the foreshock ions initially gyrated away from the thin TD. In addition, increasing the speed of the moving TD along the planar shock did not yield any noticeable differences (because there is always a TD rest frame for a planar shock); however, we expect the TD speed to be more important when the shock is curved. At later times beyond the early formation stage (e.g., after $t = 23$ gyroperiods in Figure 8.2), as the HFA grows stronger, its low-density core deforms the local shock significantly. The subsequently generated foreshock ions behave differently than those generated at the background shock. The gyromotion differences between these two

different foreshock ion populations can also generate a current that contributes to the formation of the downstream boundary of the HFA. This causes a gap to appear in the downstream boundary near the shock, seen in ion density and magnetic field changes near $x = 880$ gyroradii in Figures 8.2a and 8.2g. At a later time (not shown), another boundary starts to form, originating at the shock, and connects to the previous downstream boundary (positioned further upstream from the shock). Thus, the local shock surface is constantly changing the properties of newly reflected foreshock ions, which then go on to affect the evolution of the HFA and FB (especially when the FB forms with the ion foreshock region on both sides). This occurs in the later evolution stage, though, when the FB or HFA becomes significant enough to strongly affect the local shock. A more careful examination of this process is needed for future studies.

5. Conclusions

This paper aims to show the kinetic effects of foreshock ions interacting with a TD, that generate currents that change the magnetic field of the TD, and to understand the early formation differences between TD-driven FBs and HFAs. Using a 2-D local hybrid simulation with kinetic ions and fluid electrons, we model the early formation process of a TD-driven FB and an HFA via a moving ion-scale, finite-thickness TD interacting with a planar shock, to qualitatively examine the physics, for which we then use the injection of a foreshock ion beam to pinpoint the major physics behind the early formation processes. The injection of a foreshock ion beam provides for minimization of ULF wave growth, a way to fine-tune the properties of the foreshock ions that interact with the TD, and the ability for us to compare the early formation mechanisms of TD-driven FBs and HFAs. Our results confirm the kinetic formation model by An et al. (2020) and Liu, An, et al. (2020) and provide further details about the early formation of TD-driven FBs in comparison with the early formation of HFAs. In short, usage of a planar shock and an injection of a foreshock ion beam yield the same conclusion at the early stage, that a thin TD forms an FB and that a thick TD formed an HFA. Here we summarize their formation processes.

- The foreshock ions perform a partial gyration upon crossing the ion-scale TD, and the bulk motion differences between the foreshock ions and electron fluid lead to the generation of currents.
- The foreshock-driven currents change the magnetic field topology of the TD. The resulting magnetic field depletion within the core allows for more foreshock ions to cross the TD center and perform more drastic partial gyrations, producing stronger currents in response. This triggers the growth of the structure.
- The subsequent magnetic field changes induce electric fields that drive solar wind plasma to $\mathbf{E} \times \mathbf{B}$ drift outward, leading to an expansion of the structure. This causes the depletion of solar wind ions within the core and the pile-up of solar wind ions at the compressional boundary or boundaries.
- In the case of a thinner TD, the foreshock ions, that cross the TD, drive a stronger current, and the whole expansion process is dominated by the upstream side (an FB forms).
- For the same magnetic shear, a thicker TD causes such current to be weaker and thus comparable to the one within and downstream of the TD, resulting in two compressional boundaries and expansions in two directions (an HFA forms).
- In addition, the TD thickness also affects how much energy can be transferred from the foreshock ions. In the case of a thinner TD (FB), the foreshock ion $\mathbf{J}\cdot\mathbf{E}$ is roughly four times greater than in the case of a 16 times thicker TD (HFA).

However, the TD thickness is not the only determining factor of whether an HFA or FB forms, because in this study we only consider a situation where a TD changes the local bow shock from quasi-parallel to quasi-perpendicular. A TD with the quasi-perpendicular bow shock on both sides can still form an HFA (e.g., Giacalone & Burgess, 2010; Thomas et al., 1991), but whether it can form an FB is unknown. When the bow shock is quasi-parallel on both sides of a TD with similar θ_{Bn}, it is natural to expect that a nearly symmetric structure with two boundaries, that is, an HFA, will form regardless of TD thickness. And, unlike a TD, an RD does not have to intersect the bow shock to form an FB (e.g., Omidi et al., 2010, 2020) and an RD can also form both an HFA and an FB simultaneously when it intersects the bow shock (Omidi et al., 2020). More studies are still needed to reveal the formation differences between HFAs and FBs.

Further work remains to be tested on the early formation model using hybrid simulations. Scenarios where foreshock ions experience different TD thicknesses and magnetic shears across discontinuities (not just 90°) may reveal the early formation of ambiguous structures between FBs and HFAs. Additional factors that could affect

the formation of these structures include the initial injected parallel speeds, densities, pitch angles, and thermal speeds of foreshock ions. For example, we expect larger parallel speeds, higher densities, and larger pitch angles (thus the gyroradius is also contributed by the bulk velocity in addition to the thermal velocity) to result in stronger foreshock-driven currents, which leads to a faster growth and expansion of the structure. A future study would include a parameter scan for the preferable field and plasma conditions, like those discovered by statistical studies based on in-situ observations. Also prevalent in some of our runs involving foreshock ions with much larger parallel speeds than perpendicular speeds is the abundance of waves that originate from beam instabilities that quickly dwarf the formation of the transients. This suggests that there may be some foreshock ion parameter thresholds for the onset of formation for foreshock transients. It is also worth investigating the resulting structures that arise from a TD bounded by two quasi-parallel regions on both sides, which may easily result in two compressional boundaries. Lastly, different TD properties, such as magnetic shear angles and orientations, can also be tested in a planar shock environment to understand their effects on the early formation of TD-driven FBs and HFAs. In all, the presented simulation results pinpoint the role of foreshock ions in driving the formations of these structures within TDs; however, there is still much to discover regarding the effects of different foreshock ion and TD properties on the formation of foreshock transients.

Data Availability Statement

The simulation data used for the figures and analysis in the study are available at https://doi.org/10.6084/m9.figshare.17189438.

Acknowledgments
This work is supported by NSF AGS-1352669 and NASA grant 80NSSC18K1376. This material is also based in part upon work supported by NASA through the Alaska Space Grant Program (80NSSC20M0070). T. Z. L. is partially supported by NSF award AGS-1941012 and NASA grant 80NSSC21K1437. T. Z. L. acknowledges the NASA Living With a Star Jack Eddy Postdoctoral Fellowship Program, administered by the Cooperative Programs for the Advancement of Earth System Science (CPAESS). This work was supported in part by the high-performance computing and data storage resources operated by the Research Computing Systems Group at the University of Alaska Fairbanks Geophysical Institute.

References

An, X., Liu, T. Z., Bortnik, J., Osmane, A., & Angelopoulos, V. (2020). Formation of foreshock transients and associated secondary shocks. *The Astrophysical Journal*, *901*(1), 73. https://doi.org/10.3847/1538-4357/abaf03

Archer, M. O., Turner, D. L., Eastwood, J. P., Horbury, T. S., & Schwartz, S. J. (2014). The role of pressure gradients in driving sunward magnetosheath flows and magnetopause motion. *Journal of Geophysical Research: Space Physics*, *119*(10), 8117–8125. https://doi.org/10.1002/2014JA020342

Archer, M. O., Turner, D. L., Eastwood, J. P., Schwartz, S. J., & Horbury, T. S. (2015). Global impacts of a Foreshock Bubble: Magnetosheath, magnetopause and ground-based observations. *Planetary and Space Science*, *106*, 56–66. https://doi.org/10.1016/j.pss.2014.11.026

Billingham, L., Schwartz, S. J., & Sibeck, D. G. (2008). The statistics of foreshock cavities: Results of a Cluster survey. *Annales Geophysicae*, *26*(12), 3653–3667. https://doi.org/10.5194/angeo-26-3653-2008

Blanco-Cano, X., Kajdič, P., Omidi, N., & Russell, C. T. (2011). Foreshock cavitons for different interplanetary magnetic field geometries: Simulations and observations. *Journal of Geophysical Research*, *116*(A9), A09101. https://doi.org/10.1029/2010JA016413

Blanco-Cano, X., Omidi, N., & Russell, C. T. (2009). Global hybrid simulations: Foreshock waves and cavitons under radial interplanetary magnetic field geometry. *Journal of Geophysical Research*, *114*(A1), A01216. https://doi.org/10.1029/2008JA013406

Chu, C., Zhang, H., Sibeck, D., Otto, A., Zong, Q., Omidi, N., et al. (2017). THEMIS satellite observations of hot flow anomalies at Earth's bow shock. *Annales Geophysicae*, *35*(3), 443–451. https://doi.org/10.5194/angeo-35-443-2017

Delamere, P. A. (2006). Hybrid code simulations of the solar wind interaction with Comet 19P/Borrelly. *Journal of Geophysical Research*, *111*(A12), A12217. https://doi.org/10.1029/2006JA011859

Delamere, P. A. (2009). Hybrid code simulations of the solar wind interaction with Pluto. *Journal of Geophysical Research*, *114*(3), A03220. https://doi.org/10.1029/2008JA013756

Delamere, P. A., Swift, D. W., & Stenbaek-Nielsen, H. C. (1999). A three-dimensional hybrid code simulation of the December 1984 solar wind AMPTE release. *Geophysical Research Letters*, *26*(18), 2837–2840. https://doi.org/10.1029/1999GL900602

Eastwood, J. P., Lucek, E. A., Mazelle, C., Meziane, K., Narita, Y., Pickett, J., & Treumann, R. A. (2005). The foreshock. *Space Science Reviews*, *118*(1), 41–94. https://doi.org/10.1007/s11214-005-3824-3

Facskó, G., Németh, Z., Erdős, G., Kis, A., & Dandouras, I. (2009). A global study of hot flow anomalies using Cluster multi-spacecraft measurements. *Annales Geophysicae*, *27*(5), 2057–2076. https://doi.org/10.5194/angeo-27-2057-2009

Giacalone, J., & Burgess, D. (2010). Interaction between inclined current sheets and the heliospheric termination shock. *Geophysical Research Letters*, *37*(19), L19104. https://doi.org/10.1029/2010GL044656

Hartinger, M. D., Turner, D. L., Plaschke, F., Angelopoulos, V., & Singer, H. (2013). The role of transient ion foreshock phenomena in driving Pc5 ULF wave activity. *Journal of Geophysical Research: Space Physics*, *118*(1), 299–312. https://doi.org/10.1029/2012JA018349

Jacobsen, K. S., Phan, T. D., Eastwood, J. P., Sibeck, D. G., Moen, J. I., Angelopoulos, V., et al. (2009). THEMIS observations of extreme magnetopause motion caused by a hot flow anomaly. *Journal of Geophysical Research*, *114*(8), 1–10. https://doi.org/10.1029/2008JA013873

Kajdič, P., Blanco-Cano, X., Omidi, N., & Russell, C. T. (2011). Multi-spacecraft study of foreshock cavitons upstream of the quasi-parallel bow shock. *Planetary and Space Science*, *59*(8), 705–714. https://doi.org/10.1016/j.pss.2011.02.005

Lin, Y. (1997). Generation of anomalous flows near the bow shock by its interaction with interplanetary discontinuities. *Journal of Geophysical Research*, *102*(A11), 24265–24281. https://doi.org/10.1029/97JA01989

Lin, Y. (2002). Global hybrid simulation of hot flow anomalies near the bow shock and in the magnetosheath. *Planetary and Space Science*, *50*(5–6), 577–591. https://doi.org/10.1016/S0032-0633(02)00037-5

Liu, T. Z., An, X., Zhang, H., & Turner, D. (2020). Magnetospheric multiscale observations of foreshock transients at their very early stage. *The Astrophysical Journal*, *902*(1), 5. https://doi.org/10.3847/1538-4357/abb249

Liu, T. Z., Angelopoulos, V., Hietala, H., & Wilson, L. B., III. (2017). Statistical study of particle acceleration in the core of foreshock transients. *Journal of Geophysical Research: Space Physics*, *122*(7), 7197–7208. https://doi.org/10.1002/2017JA024043

Liu, T. Z., Angelopoulos, V., & Lu, S. (2019). Relativistic electrons generated at Earth's quasi-parallel bow shock. *Science Advances*, *5*(7). https://doi.org/10.1126/sciadv.aaw1368

Liu, T. Z., Hietala, H., Angelopoulos, V., & Turner, D. L. (2016). Observations of a new foreshock region upstream of a foreshock bubble's shock. *Geophysical Research Letters*, *43*(10), 4708–4715. https://doi.org/10.1002/2016GL068984

Liu, T. Z., Lu, S., Angelopoulos, V., Hietala, H., & Wilson, L. B. (2017). Fermi acceleration of electrons inside foreshock transient cores. *Journal of Geophysical Research: Space Physics*, *122*(9), 9248–9263. https://doi.org/10.1002/2017JA024480

Liu, T. Z., Lu, S., Angelopoulos, V., Lin, Y., & Wang, X. Y. (2018). Ion acceleration inside foreshock transients. *Journal of Geophysical Research: Space Physics*, *123*(1), 163–178. https://doi.org/10.1002/2017JA024838

Liu, T. Z., Lu, S., Turner, D. L., Gingell, I., Angelopoulos, V., Zhang, H., et al. (2020). Magnetospheric Multiscale (MMS) observations of magnetic reconnection in foreshock transients. *Journal of Geophysical Research: Space Physics*, *125*(4), e2020JA027822. https://doi.org/10.1029/2020JA027822

Liu, T. Z., Turner, D. L., Angelopoulos, V., & Omidi, N. (2016). Multipoint observations of the structure and evolution of foreshock bubbles and their relation to hot flow anomalies. *Journal of Geophysical Research: Space Physics*, *121*(6), 5489–5509. https://doi.org/10.1002/2016JA022461

Liu, T. Z., Zhang, H., Wang, C., Angelopoulos, V., Vu, A., Wang, X., & Lin, Y. (2021). Statistical study of foreshock transients in the midtail foreshock. *Journal of Geophysical Research: Space Physics*, *126*(5), e2021JA029156. https://doi.org/10.1029/2021JA029156

Liu, Z., Turner, D. L., Angelopoulos, V., & Omidi, N. (2015). THEMIS observations of tangential discontinuity-driven foreshock bubbles. *Geophysical Research Letters*, *42*(19), 7860–7866. https://doi.org/10.1002/2015GL065842

Lucek, E. A., Horbury, T. S., Balogh, A., & Dandouras, I. (2004). Cluster observations of hot flow anomalies. *Journal of Geophysical Research*, *109*(A6), A06207. https://doi.org/10.1029/2003JA010016

Omidi, N., Eastwood, J. P., & Sibeck, D. G. (2010). Foreshock bubbles and their global magnetospheric impacts. *Journal of Geophysical Research*, *115*(A6), A06204. https://doi.org/10.1029/2009JA014828

Omidi, N., Lee, S. H., & Sibeck, D. G. (2021). Ion acceleration by foreshock bubbles. *Journal of Geophysical Research: Space Physics*, *126*(5), 1–17. https://doi.org/10.1029/2020JA028924

Omidi, N., Lee, S. H., Sibeck, D. G., Turner, D. L., Liu, T. Z., & Angelopoulos, V. (2020). Formation and topology of foreshock bubbles. *Journal of Geophysical Research: Space Physics*, *125*(9), e2020JA028058. https://doi.org/10.1029/2020JA028058

Omidi, N., & Sibeck, D. G. (2007). Formation of hot flow anomalies and solitary shocks. *Journal of Geophysical Research*, *112*(A1), A01203. https://doi.org/10.1029/2006JA011663

Omidi, N., Zhang, H., Sibeck, D., & Turner, D. (2013). Spontaneous hot flow anomalies at quasi-parallel shocks: 2. Hybrid simulations. *Journal of Geophysical Research: Space Physics*, *118*(1), 173–180. https://doi.org/10.1029/2012JA018099

Paschmann, G., Haerendel, G., Sckopke, N., Möbius, E., Lühr, H., & Carlson, C. W. (1988). Three-dimensional plasma structures with anomalous flow directions near the Earth's bow shock. *Journal of Geophysical Research*, *93*(A10), 11279. https://doi.org/10.1029/JA093iA10p11279

Schwartz, S. (1995). Hot flow anomalies near the Earth's bow shock. *Advances in Space Research*, *15*(8–9), 107–116. https://doi.org/10.1016/0273-1177(94)00092-F

Schwartz, S. J., Avanov, L., Turner, D., Zhang, H., Gingell, I., Eastwood, J. P., et al. (2018). Ion kinetics in a hot flow anomaly: MMS observations. *Geophysical Research Letters*, *45*(21), 11520–11529. https://doi.org/10.1029/2018GL080189

Schwartz, S. J., Burgess, D., Wilkinson, W. P., Kessel, R. L., Dunlop, M., & Lühr, H. (1992). Observations of short large-amplitude magnetic structures at a quasi-parallel shock. *Journal of Geophysical Research*, *97*(A4), 4209. https://doi.org/10.1029/91JA02581

Schwartz, S. J., Chaloner, C. P., Christiansen, P. J., Coates, A. J., Hall, D. S., Johnstone, A. D., et al. (1985). An active current sheet in the solar wind. *Nature*, *318*(6043), 269–271. https://doi.org/10.1038/318269a0

Schwartz, S. J., Paschmann, G., Sckopke, N., Bauer, T. M., Dunlop, M., Fazakerley, A. N., & Thomsen, M. F. (2000). Conditions for the formation of hot flow anomalies at Earth's bow shock. *Journal of Geophysical Research*, *105*(A6), 12639–12650. https://doi.org/10.1029/1999JA000320

Sibeck, D. G., Borodkova, N. L., Schwartz, S. J., Owen, C. J., Kessel, R., Kokubun, S., et al. (1999). Comprehensive study of the magnetospheric response to a hot flow anomaly. *Journal of Geophysical Research*, *104*(A3), 4577–4593. https://doi.org/10.1029/1998JA900021

Sibeck, D. G., Phan, T.-D., Lin, R., Lepping, R. P., & Szabo, A. (2002). Wind observations of foreshock cavities: A case study. *Journal of Geophysical Research*, *107*(A10), 1271. https://doi.org/10.1029/2001JA007539

Swift, D. W. (1995). Use of a hybrid code to model the Earth's magnetosphere. *Geophysical Research Letters*, *22*(3), 311–314. https://doi.org/10.1029/94GL03082

Swift, D. W. (1996). Use of a hybrid code for global-scale plasma simulation. *Journal of Computational Physics*, *126*(1), 109–121. https://doi.org/10.1006/jcph.1996.0124

Thomas, V. A., Winske, D., Thomsen, M. F., & Onsager, T. G. (1991). Hybrid simulation of the formation of a hot flow anomaly. *Journal of Geophysical Research*, *96*(A7), 11625. https://doi.org/10.1029/91JA01092

Thomsen, M. F., Gosling, J. T., Fuselier, S. A., Bame, S. J., & Russell, C. T. (1986). Hot, diamagnetic cavities upstream from the Earth's bow shock. *Journal of Geophysical Research*, *91*(A3), 2961. https://doi.org/10.1029/JA091iA03p02961

Turner, D. L., Liu, T. Z., Wilson, L. B., Cohen, I. J., Gershman, D. G., Fennell, J. F., et al. (2020). Microscopic, multipoint characterization of foreshock bubbles with Magnetospheric Multiscale (MMS). *Journal of Geophysical Research: Space Physics*, *125*(7), e2019JA027707. https://doi.org/10.1029/2019JA027707

Turner, D. L., Omidi, N., Sibeck, D. G., & Angelopoulos, V. (2013). First observations of foreshock bubbles upstream of Earth's bow shock: Characteristics and comparisons to HFAs. *Journal of Geophysical Research: Space Physics*, *118*(4), 1552–1570. https://doi.org/10.1002/jgra.50198

Turner, D. L., Wilson, L. B., Liu, T. Z., Cohen, I. J., Schwartz, S. J., Osmane, A., et al. (2018). Autogenous and efficient acceleration of energetic ions upstream of Earth's bow shock. *Nature*, *561*(7722), 206–210. https://doi.org/10.1038/s41586-018-0472-9

Wang, B., Liu, T., Nishimura, Y., Zhang, H., Hartinger, M., Shi, X., et al. (2020). Global propagation of magnetospheric Pc5 ULF waves driven by foreshock transients. *Journal of Geophysical Research: Space Physics*, *125*(12), 1–20. https://doi.org/10.1029/2020JA028411

Wang, B., Zhang, H., Liu, Z., Liu, T., Li, X., & Angelopoulos, V. (2021). Energy Modulations of Magnetospheric Ions Induced by Foreshock Transient-Driven Ultralow-Frequency Waves. *Geophysical Research Letters*, *48*(10), 1–11. https://doi.org/10.1029/2021GL093913

Wang, C. P., Wang, X., Liu, T. Z., & Lin, Y. (2021). A foreshock bubble driven by an IMF tangential discontinuity: 3D global hybrid simulation. *Geophysical Research Letters*, *48*(9), e2021GL093068. https://doi.org/10.1029/2021GL093068

Wang, S., Zong, Q., & Zhang, H. (2012). Cases and statistical study on Hot Flow Anomalies with Cluster spacecraft data. *Science China Technological Sciences*, *55*(5), 1402–1418. https://doi.org/10.1007/s11431-012-4767-z

Wilson, L. B., Sibeck, D. G., Turner, D. L., Osmane, A., Caprioli, D., & Angelopoulos, V. (2016). Relativistic electrons produced by foreshock disturbances observed upstream of Earth's bow shock. *Physical Review Letters*, *117*(21), 215101. https://doi.org/10.1103/PhysRevLett.117.215101

Zhang, H., Sibeck, D. G., Zong, Q.-G., Omidi, N., Turner, D., & Clausen, L. B. N. (2013). Spontaneous hot flow anomalies at quasi-parallel shocks: 1. Observations. *Journal of Geophysical Research: Space Physics*, *118*(6), 3357–3363. https://doi.org/10.1002/jgra.50376

Zhang, H., Zong, Q.-G., Connor, H., Delamere, P., Facskó, G., Han, D.-S., et al. (2022). Dayside transient phenomena and their impact on the magnetosphere and ionosphere. *Space Science Reviews*. https://doi.org/10.1007/s11214-021-00865-0

Zhao, L. L., Zhang, H., & Zong, Q. G. (2017). A statistical study on hot flow anomaly current sheets. *Journal of Geophysical Research: Space Physics*, *122*(1), 235–248. https://doi.org/10.1002/2016ja023319

Zhao, L. L., Zong, Q. G., Zhang, H., & Wang, S. (2015). Case and statistical studies on the evolution of hot flow anomalies. *Journal of Geophysical Research: Space Physics*, *120*(8), 6332–6346. https://doi.org/10.1002/2014JA020862